

# The LHC as a Neutrino-Ion Collider

Juan M. Cruz-Martinez<sup>1</sup>, Max Fieg<sup>2</sup>, Tommaso Giani<sup>3,4</sup>, Peter Krack<sup>3,4</sup>, Toni Mäkelä<sup>5</sup>, Tanjona R. Rabemananjara<sup>3,4</sup>, Juan Rojo<sup>3,4</sup>

<sup>1</sup> CERN, Theoretical Physics Department, CH-1211 Geneva 23, Switzerland

<sup>2</sup> Department of Physics and Astronomy, University of California, Irvine, CA 92697 USA

<sup>3</sup> Department of Physics and Astronomy, Vrije Universiteit, NL-1081 HV Amsterdam

<sup>4</sup> Nikhef Theory Group, Science Park 105, 1098 XG Amsterdam, The Netherlands

<sup>5</sup> National Centre for Nuclear Research, Pasteura 7, Warsaw, PL-02-093, Poland

Received: date / Revised version: date

**Abstract.** Proton-proton collisions at the LHC generate a high-intensity collimated beam of neutrinos in the forward (beam) direction, characterised by energies of up to several TeV. The recent observation of LHC neutrinos by FASER $\nu$  and SND@LHC signals that this hitherto ignored particle beam is now available for scientific inquiry. Here we quantify the impact that neutrino deep-inelastic scattering (DIS) measurements at the LHC would have on the parton distributions (PDFs) of protons and heavy nuclei. We generate projections for DIS structure functions for FASER $\nu$  and SND@LHC at Run III, as well as for the FASER $\nu$ 2, AdvSND, and FLArE experiments to be hosted at the proposed Forward Physics Facility (FPF) operating concurrently with the High-Luminosity LHC (HL-LHC). We determine that up to one million electron- and muon-neutrino DIS interactions within detector acceptance can be expected by the end of the HL-LHC, covering a kinematic region in  $x$  and  $Q^2$  overlapping with that of the Electron-Ion Collider. Including these DIS projections into global (n)PDF analyses, specifically PDF4LHC21, NNPDF4.0, and EPPS21, reveals a significant reduction of PDF uncertainties, in particular for strangeness and the up and down valence PDFs. We show that LHC neutrino data enables improved theoretical predictions for core processes at the HL-LHC, such as Higgs and weak gauge boson production. Our analysis demonstrates that exploiting the LHC neutrino beam effectively provides CERN with a “Neutrino-Ion Collider” without requiring modifications in its accelerator infrastructure.

**PACS.** 12.38.-t Quantum chromodynamics – 24.85.+p Quarks, gluons, and QCD in nuclear reactions

## Contents

1	Introduction and motivation . . . . .	1
2	Deep-inelastic scattering with LHC neutrinos . . . . .	2
2.1	Neutrino DIS revisited . . . . .	2
2.2	LHC far-forward neutrino experiments . . . . .	4
	Detector overview. . . . .	4
	FASER $\nu$ . . . . .	4
	SND@LHC. . . . .	4
	FASER $\nu$ 2. . . . .	4
	AdvSND. . . . .	5
	FLArE. . . . .	5
2.3	Differential scattering event rates . . . . .	6
2.4	Statistical and systematic uncertainties . . . . .	8
2.5	Pseudo-data generation . . . . .	11
2.6	PDF impact assessment . . . . .	13
3	Constraints on proton and nuclear structure . . . . .	13
3.1	Proton PDFs: impact on PDF4LHC21 . . . . .	13
	Constraints from FASER $\nu$ 2. . . . .	13
	Relevance of charm-tagged measurements. . . . .	15
	Lepton-charge identification. . . . .	15
	Experiment dependence. . . . .	15
	Combined impact of the FPF experiments. . . . .	15

3.2	Proton PDFs: impact on NNPDF4.0 . . . . .	16
3.3	Nuclear PDFs: impact on EPPS21 . . . . .	19
4	Implications for Higgs and weak boson production . . . . .	21
5	Summary and outlook . . . . .	27
A	Impact of FASER $\nu$ Run III measurements . . . . .	28
B	Additional nPDF impact studies . . . . .	28

## 1 Introduction and motivation

Proton-proton collisions at the LHC produce a high-intensity collimated flux of neutrinos. These neutrinos are characterised by the largest energies ever achieved in laboratory experiments, reaching up to several TeV [1]. Due to the lack of dedicated instrumentation in the far-forward region, until recently these neutrinos avoided detection. The recent observation of LHC neutrinos [2–4] by the FASER [5, 6] and SND@LHC [7, 8] far-forward experiments demonstrates that this hitherto discarded beam can now be deployed for physics studies. Beyond the ongoing Run III, a dedicated suite of upgraded far-forward neutrino experiments

would be hosted by the proposed Forward Physics Facility (FPF) [9, 10] operating concurrently with the High-Luminosity LHC (HL-LHC) [11, 12]. Current and future LHC neutrino experiments enable unprecedented scientific opportunities for particle and astroparticle physics both within the Standard Model and beyond it, as summarised in [9, 10] and references therein.

Measurements of neutrino structure functions [13–15] in deep-inelastic scattering (DIS) are sensitive probes of the parton distributions (PDFs) of nucleons and nuclei [16–18], in particular concerning (anti)quark flavour separation and strangeness [19–22]. Constraints arising from charged-current neutrino scattering provide information on complementary flavour combinations as compared to neutral-current charged-lepton DIS. Several experiments have measured neutrino DIS structure functions over a wide range of energies, and neutrino data from CHORUS [23], NuTeV [24], CCFR [25], NOMAD [26], CDHS [27], and other experiments is routinely included in global determinations of proton [28–30] and nuclear PDFs [31–33].

As compared to previous neutrino DIS experiments, neutrino scattering at the LHC involves energies of up to a factor 10 higher. Furthermore, large event rates are expected, with up to one million muon neutrinos interacting at the FPF detectors [9, 10]. Initial estimates [10] indicate that an extension of the coverage of available neutrino DIS data by an order of magnitude both at small- $x$  and large- $Q^2$  should be possible. However, quantitative projections for the kinematic reach and experimental accuracy expected at current and future LHC neutrino experiments are not available. The lack of these projections has prevented detailed studies assessing the impact of LHC neutrino data in global analyses of proton and nuclear PDFs, comparable to those performed for the HL-LHC [11, 34], the Electron-Ion Collider (EIC) [35–37], and the Large Hadron-electron Collider (LHeC) [38–40].

Here we bridge this gap by quantifying the expected impact of LHC neutrino structure functions on proton and nuclear PDFs. To this end, we produce simulations for FASER $\nu$  and SND@LHC at Run III as well as for the proposed FPF experiments [9, 10, 41, 42], FLArE, AdvSND, and FASER $\nu$ 2. For each experiment, we determine the expected event yields in bins of  $(x, Q^2, E_\nu)$  satisfying acceptance and selection cuts, generate pseudo-data for inclusive and charm structure functions, and estimate their dominant systematic uncertainties. Subsequently, we study their impact on the proton and nuclear PDFs by means of both the Hessian profiling [34, 43–45] of PDF4LHC21 [46] (for protons) and EPPS21 [31] (for tungsten nuclei) within the xFITTER [47–50] open-source QCD analysis framework, as well as with the direct inclusion in the open-source NNPDF4.0 fitting code [51].

Our analysis reveals that LHC neutrino structure functions can provide stringent constraints on the light quark and antiquark PDFs, especially on the up and down valence quarks and on strangeness, as compared to state-of-the-art global analyses. We also find that accounting for the main systematic uncertainties does not significantly degrade the sensitivity achieved in the baseline fits considering only

statistical errors. We quantify the impact in our results of charm-tagged structure functions (large), study the relevance of final-state lepton-charge identification capabilities (moderate), and compare the constraints provided by different experiments (finding that the overall sensitivity is dominated by FASER $\nu$ 2). We also study the implications of the resulting improvement in PDF precision on core processes at the HL-LHC, finding a theory error reduction of up to a factor two in the most optimistic scenario for selected Higgs and gauge boson production cross-sections.

Our results demonstrate that the availability of far-forward neutrino detectors at the LHC effectively provides CERN with a charged-current counterpart of the EIC, with similar kinematic reach and complementary sensitivity on hadronic structure. Therefore, LHC neutrino experiments realise, upon Lorentz-boosting, the analog of a “Neutrino-Ion Collider” at CERN without the need of new accelerator infrastructure or additional energy consumption.

The outline of this paper is as follows. Sect. 2 describes the procedure adopted to generate projections for neutrino DIS structure functions at the LHC and the methodology used to include these into PDF fits. The impact of such LHC structure function measurements on proton and nuclear PDFs is quantified in Sect. 3, with the associated implications for precision phenomenology at the HL-LHC assessed in Sect. 4. We summarise in Sect. 5, where we also consider possible directions for follow-up research. Additional results are collected in two appendices: App. A studies the constraints provided by FASER $\nu$  measurements at Run III, and App. B quantifies the stability of the nPDF impact projections with respect to input variations.

## 2 Deep-inelastic scattering with LHC neutrinos

Here we describe the procedure adopted to generate projections for the kinematic coverage and uncertainties associated to measurements of neutrino-nucleus scattering at the LHC far-forward experiments. First, we summarise the theoretical description of differential neutrino scattering in terms of DIS structure functions. Then, we present an overview of the operative and proposed LHC far-forward neutrino detectors that are considered in the present study and indicate their acceptance and performance parameters. By convoluting the expected electron and muon neutrino fluxes with the acceptance and scattering rates of each of these detectors, we evaluate the event yields in bins of  $x$ ,  $Q^2$ , and  $E_\nu$ , and the associated statistical and systematic uncertainties. Finally, we discuss the procedure adopted to generate pseudo-data for LHC neutrino structure functions and to quantify their impact into proton and nuclear PDF determinations.

### 2.1 Neutrino DIS revisited

The double-differential cross-section for neutrino-nucleus charged-current scattering, see [15] and references therein,

can be expressed in terms of three independent structure functions  $F_2^{\nu A}$ ,  $xF_3^{\nu A}$  and  $F_L^{\nu A}$ :

$$\frac{d^2\sigma^{\nu A}(x, Q^2, y)}{dxdy} = \frac{G_F^2 s / 4\pi}{(1 + Q^2/m_W^2)^2} \quad (2.1)$$

$$[Y_+ F_2^{\nu A}(x, Q^2) - y^2 F_L^{\nu A}(x, Q^2) + Y_- x F_3^{\nu A}(x, Q^2)],$$

where  $Y_{\pm} = 1 \pm (1 - y)^2$  and with a counterpart expression for anti-neutrino scattering,

$$\frac{d^2\sigma^{\bar{\nu} A}(x, Q^2, y)}{dxdy} = \frac{G_F^2 s / 4\pi}{(1 + Q^2/m_W^2)^2} \quad (2.2)$$

$$[Y_+ F_2^{\bar{\nu} A}(x, Q^2) - y^2 F_L^{\bar{\nu} A}(x, Q^2) - Y_- x F_3^{\bar{\nu} A}(x, Q^2)],$$

with  $s = 2m_N E_{\nu}$  being the neutrino-nucleon centre-of-mass energy squared,  $m_N$  the nucleon mass,  $E_{\nu}$  the incoming neutrino energy, and  $y = Q^2/(2xm_N E_{\nu})$  the inelasticity. In the case of tau-neutrino scattering, tau-lepton mass effects may be relevant and Eqns. (2.1) and (2.2) receive additional contributions from the  $F_4$  and  $F_5$  structure functions. We neglect these effects, since here we focus on electron and muon neutrino scattering.

Structure functions depend on both  $x$  and  $Q^2$ , while the differential cross-section depends also on the neutrino energy  $E_{\nu}$ , or alternatively on the inelasticity  $y$ . Further, structure functions  $F_i^{\nu A}(x, Q^2)$  and  $F_i^{\bar{\nu} A}(x, Q^2)$  depend on the nuclear target  $A$  entering neutrino scattering through the nuclear modifications of the free-nucleon PDFs. Eqns. (2.1) and (2.2) are valid provided the hadronic invariant mass  $W$  is above the resonance production threshold,

$$W^2 = \left( m_N^2 + Q^2 \frac{(1-x)}{x} \right) \gtrsim (2 \text{ GeV})^2. \quad (2.3)$$

In addition, here we restrict ourselves to the DIS region with perturbative momentum transfers  $Q^2 \gtrsim 2 \text{ GeV}^2$ , such that the structure functions can be decomposed as

$$F_i^{\nu A}(x, Q^2) = \sum_{j=q,\bar{q},g} \int_x^1 \frac{dz}{z} C_{i,j}^{\nu N}(z, \alpha_s(Q^2)) f_j^{(A)}\left(\frac{x}{z}, Q^2\right),$$

$$\text{with } i = 2, 3, L, \quad (2.4)$$

expressed in terms of a convolution of partonic scattering cross-sections  $C_{i,j}^{\nu N}(x, \alpha_s)$  and of process-independent PDFs  $f_j^{(A)}(x, Q^2)$ . A similar expression holds for charm production [21], which requires accounting also for charm mass effects [52]. Here the theory pipeline adopted to evaluate neutrino structure functions using Eq. (2.4) is provided by EKO [53] and YADISM [15, 54] interfaced to PINEAPPL [55] for the generation of fast interpolation grids.

Different neutrino structure functions provide complementary sensitivity to the partonic flavour decompositions of nucleons. To illustrate this feature, consider a leading order calculation for a proton target with  $n_f = 4$  active quark flavours, a diagonal CKM matrix, and no heavy quark mass effects. The resulting  $F_2^{\nu p}$  and  $x F_3^{\nu p}$  structure

functions read

$$F_2^{\nu p}(x, Q^2) = 2x(f_{\bar{u}} + f_d + f_s + f_{\bar{c}})(x, Q^2),$$

$$F_2^{\bar{\nu} p}(x, Q^2) = 2x(f_u + f_{\bar{d}} + f_{\bar{s}} + f_c)(x, Q^2), \quad (2.5)$$

$$xF_3^{\nu p}(x, Q^2) = 2x(-f_{\bar{u}} + f_d + f_s - f_{\bar{c}})(x, Q^2),$$

$$xF_3^{\bar{\nu} p}(x, Q^2) = 2x(f_u - f_{\bar{d}} - f_{\bar{s}} + f_c)(x, Q^2).$$

The corresponding expressions for a neutron target are obtained from isospin symmetry

$$F_2^{\nu n}(x, Q^2) = 2x(f_{\bar{d}} + f_u + f_s + f_{\bar{c}})(x, Q^2),$$

$$F_2^{\bar{\nu} n}(x, Q^2) = 2x(f_d + f_{\bar{u}} + f_{\bar{s}} + f_c)(x, Q^2), \quad (2.6)$$

$$xF_3^{\nu n}(x, Q^2) = 2x(-f_{\bar{d}} + f_u + f_s - f_{\bar{c}})(x, Q^2),$$

$$xF_3^{\bar{\nu} n}(x, Q^2) = 2x(f_d - f_{\bar{u}} - f_{\bar{s}} + f_c)(x, Q^2),$$

while for an isoscalar, free-nucleon target denoted by  $N$  one has

$$F_2^{\nu N}(x, Q^2) = 2x(f_{u+} + f_{d+} + 2f_s + 2f_{\bar{c}})(x, Q^2),$$

$$F_2^{\bar{\nu} N}(x, Q^2) = 2x(f_{u+} + f_{d+} + 2f_{\bar{s}} + 2f_c)(x, Q^2), \quad (2.7)$$

$$xF_3^{\nu N}(x, Q^2) = 2x(f_{u-} + f_{d-} + 2f_s - 2f_{\bar{c}})(x, Q^2),$$

$$xF_3^{\bar{\nu} N}(x, Q^2) = 2x(f_{u-} + f_{d-} - 2f_{\bar{s}} + 2f_c)(x, Q^2),$$

in terms of the valence and sea PDF combinations defined by the following relations

$$f_{q+}(x, Q^2) \equiv (f_q + f_{\bar{q}})(x, Q^2),$$

$$f_{q-}(x, Q^2) \equiv (f_q - f_{\bar{q}})(x, Q^2). \quad (2.8)$$

We note that, even for isoscalar targets, separate measurements for neutrinos and antineutrinos will not be equivalent, since in general the strange and charm sea asymmetries  $f_{s-}$  and  $f_{c-}$  are not expected to vanish [56, 57].

In the projections presented here, when interpreting the LHC neutrino structure functions in terms of proton PDFs, we will assume an isoscalar free-nucleon target and neglect nuclear PDF modifications, along the lines of Eq. (2.7). Accounting for nuclear modifications in a global proton PDF fit is possible by means of the procedure developed in [58, 59] based on the theory covariance matrix approach [60, 61]. On the other hand, when evaluating structure functions for a tungsten (W) target, we keep into account both nuclear corrections and that the target is not isoscalar when evaluating the physical observables.

It is also illustrative to compare the PDF dependence of neutrino structure functions at LO with that of their counterparts for neutral-current scattering with a charged lepton projectile. Within the same assumptions, for energies below the  $Z$ -boson mass,  $Q^2 \ll m_Z^2$ , the corresponding decomposition is

$$F_2^{\ell p}(x, Q^2) = x \left( \frac{4}{9} [f_{u+} + f_{c+}] + \frac{1}{9} [f_{d+} + f_{s+}] \right) (x, Q^2),$$

$$F_2^{\ell n}(x, Q^2) = x \left( \frac{4}{9} [f_{d+} + f_{c+}] + \frac{1}{9} [f_{u+} + f_{s+}] \right) (x, Q^2),$$

$$F_2^{\ell N}(x, Q^2) = x \left( \frac{5}{18} [f_{u+} + f_{d+}] + \frac{1}{9} f_{s+} + \frac{4}{9} f_{c+} \right) (x, Q^2), \quad (2.9)$$

with  $xF_3$  being negligible in this region. Comparing Eqns. (2.5)–(2.7) with Eq. (2.9) showcases the complementarity between neutrino and charged-lepton DIS in terms of sensitivity to different flavour PDF combinations. This implies that the best sensitivity on the quark flavour separation in the nucleon would be provided by combining neutrino DIS from the LHC far-forward experiments with measurements on charged-lepton DIS at the EIC.

## 2.2 LHC far-forward neutrino experiments

The calculation of differential neutrino scattering event rates at the LHC far-forward detectors involves two main ingredients: the energy and flavour dependence of the incoming neutrino flux crossing the detector fiducial volume, on the one hand, and the scattering rates within the detector acceptance, on the other hand. Here we summarise the main features of the existing and future far-forward detectors considered, in particular concerning their acceptance and expected performance. We focus on muon-neutrino scattering, which benefits from the highest rates and is less affected by theoretical uncertainties in the production mechanism, but provide also predictions for the subdominant electron-neutrino structure functions.

The kinematics of a charged-current neutrino DIS event  $(x, Q^2, E_\nu)$ , or alternatively  $(x, Q^2, y)$ , are uniquely specified by the measurement of three independent final-state variables, such as  $(E_\ell, \theta_\ell, W^2)$  or  $(E_\ell, \theta_\ell, E_h)$ , with  $E_\ell$  and  $\theta_\ell$  being the energy and polar angle of the outgoing charged lepton and  $E_h$  the total energy of the hadronic final state. Most neutrino detectors can only access  $E_h$ , given that measuring the invariant mass  $W^2$  requires fully reconstructing the final state. A measurement of the three kinematic variables  $(E_\ell, \theta_\ell, E_h)$  then fixes the DIS kinematics as:

$$\begin{aligned} E_\nu &= E_h + E_\ell, \\ Q^2 &= 4(E_h + E_\ell)E_\ell \sin^2(\theta_\ell/2), \\ x &= \frac{4(E_h + E_\ell)E_\ell \sin^2(\theta_\ell/2)}{2m_N E_h}. \end{aligned} \quad (2.10)$$

These relations also reflect how systematic uncertainties affecting the measurement of  $(E_\ell, \theta_\ell, E_h)$  translate into uncertainties in the reconstructed values of  $(x, Q^2, E_\nu)$  modifying the expected binned event rates.

**Detector overview.** Table 2.1 summarises, for each of the far-forward LHC neutrino experiments considered in this work, their pseudo-rapidity coverage, target material, whether they can identify the sign of the outgoing charged lepton, the acceptance for the charged lepton and hadronic final state, and the expected reconstruction performance. We consider separately acceptance and performance for electron-neutrinos and muon-neutrinos. In these projections we assume that FASER $\nu$  and SND@LHC acquire data for Run III ( $\mathcal{L} = 150 \text{ fb}^{-1}$ ), while FASER $\nu$ 2, AdvSND, and FLArE take data for the complete HL-LHC period ( $\mathcal{L} = 3 \text{ ab}^{-1}$ ). In the case of FLArE, we consider projections for fiducial volumes corresponding to both 10 and

100 tonne detectors. In the following, we provide details about the information collected in Table 2.1.

**FASER $\nu$ .** The ForwArd Search ExpeRiment (FASER) detector and its companion FASER $\nu$  [2, 5, 6, 62] are located at the TI12 tunnel of the CERN accelerator complex. Both detectors are aligned with the collision axis line-of-sight (LOS) and have been acquiring data since the beginning of Run III in 2022. Neutrino scattering takes place in the FASER $\nu$  detector, composed by interleaved emulsion and tungsten plates and adding up to a mass of 1.1 tonnes with a fiducial volume of  $20 \text{ cm} \times 25 \text{ cm} \times 80 \text{ cm}$ . The FASER apparatus is immersed in a magnetic field, providing charged-lepton identification thanks to two 1 m-long dipole magnets with  $B = 0.57 \text{ T}$  and another 1.5 m-long magnet in front of the spectrometer. Neutrino detection and identification can be carried out either using the emulsion films, which have the key benefit of excellent position and angular resolution, or instead using the electronic detector components of FASER, which enable the tagging of the outgoing downstream energetic muons. FASER $\nu$  is sensitive to neutrinos with pseudorapidity  $\eta_\nu \geq 8.5$  and can also identify charm-tagged events. To identify the charge of the lepton from a neutrino interaction, the lepton is required to pass through the FASER spectrometer. This imposes an angular requirement on the outgoing charged lepton, indicated in Table 2.1. Also, to identify a DIS interaction the emulsion detector requires at least 5 charged tracks to emerge from the interaction vertex. We implement this last constraint in our simulations by requiring a minimum hadronic energy when calculating the event yields, as the charged track multiplicity is expected to grow with  $W$  [5, 63].

**SND@LHC.** In the same manner as FASER, the SND@LHC experiment [8] is located in a service tunnel (TI18) around 500 meters from the ATLAS interaction point and has been taking data since the beginning of Run III. SND@LHC is installed off the LOS axis in order to cover the neutrino pseudo-rapidity range of  $7.2 \leq \eta_\nu \leq 8.4$ . With a total fiducial volume corresponding to a 830 kg detector with a length of 35 cm, it is composed by tungsten plates, where neutrino scattering takes place, interleaved with nuclear emulsions and electronic tracker components. Downstream, the scattering volume is followed by a hadronic calorimeter and a muon tracking system. The electromagnetic and hadronic energy deposits can be measured at the electronic detectors, with the emulsion components providing vertex reconstruction. The lack of magnetic field prevents the charge-sign identification of the outgoing charged leptons.

**FASER $\nu$ 2.** This is a proposed 20-tonne neutrino experiment located on the LOS of the LHC neutrino beam to be installed in the FPF cavern. It is based on the same technology as FASER $\nu$ , and hence relies on a emulsion-based detector optimised to identify heavy flavour particles,

Detector	Rapidity	Target	Charge ID	Acceptance	Performance
FASER $\nu$	$\eta_\nu \geq 8.5$	Tungsten (1.1 tonnes)	muons	$E_\ell, E_h \gtrsim 100 \text{ GeV}$	$\delta E_\ell \sim 30\%$
				$\tan \theta_\ell \lesssim 0.025$ (charge ID)	$\delta \theta_\ell \sim 0.06 \text{ mrad}$
				reco $E_h$ & charm ID	$\delta E_h \sim 30\%$
SND@LHC	$7.2 \leq \eta_\nu \leq 8.4$	Tungsten (0.83 tonnes)	n/a	$E_\ell, E_h \gtrsim 20 \text{ GeV}$ $\theta_\mu \lesssim 0.15, \theta_e \lesssim 0.5$	n/a
FASER $\nu$ 2	$\eta_\nu \geq 8.5$	Tungsten (20 tonnes)	muons	$E_\ell, E_h \gtrsim 100 \text{ GeV}$	$\delta E_\ell \sim 30\%$
				$\tan \theta_\ell \lesssim 0.05$ (charge ID)	$\delta \theta_\ell \sim 0.06 \text{ mrad}$
				reco $E_h$ & charm ID	$\delta E_h \sim 30\%$
AdvSND-far	$7.2 \leq \eta_\nu \leq 8.4$	Tungsten (5 tonnes)	muons	$E_\ell, E_h \gtrsim 20 \text{ GeV}$	n/a
				$\theta_\mu \lesssim 0.15, \theta_e \lesssim 0.5$	
				reco $E_h$	
FLArE (*)	$\eta_\nu \geq 7.5$	LAr (10, 100 tonnes)	muons	$E_\ell, E_h \gtrsim 2 \text{ GeV}, E_e \lesssim 2 \text{ TeV}$	$\delta E_e \sim 5\%, \delta E_\mu \sim 30\%$
				$\theta_\mu \lesssim 0.025, \theta_e \lesssim 0.5$	$\delta \theta_\ell \sim 15 \text{ mrad}$
				reco $E_h$	$\delta E_h \sim 30\%$

**Table 2.1.** For each of the far-forward LHC neutrino experiments considered, we indicate their neutrino pseudo-rapidity coverage, target material, whether they can identify the sign of the outgoing charged lepton, the acceptance for the charged lepton and hadronic final state, and the expected reconstruction performance. We consider separately acceptance and performance for electron and muon neutrinos. For FLArE, we assume that muons would be measured in the FASER2 spectrometer situated downstream in the FPF cavern. See the description of each experiment in the text for more details. For our projections we assume that FASER $\nu$  and SND@LHC acquire data for the Run III period ( $\mathcal{L} = 150 \text{ fb}^{-1}$ ), while FASER $\nu$ 2, AdvSND, and FLArE take data for the complete HL-LHC period ( $\mathcal{L} = 3 \text{ ab}^{-1}$ ). In the case of FLArE, we consider projections for fiducial volumes corresponding to both 10 and 100 tonne detectors, which we denote for the two detectors as as FLArE(\*)).

including tau leptons and charm and beauty particles, arising from neutrino interactions. It would be sensitive to neutrinos with pseudorapidity  $\eta_\nu \geq 8.5$ . The FASER $\nu$ 2 detector is composed of 3300 emulsion layers interleaved with 2-mm-thick tungsten plates, for a total volume of tungsten of  $40 \text{ cm} \times 40 \text{ cm} \times 6.6 \text{ m}$ . The combination of FASER $\nu$ 2 with the nearby FASER2 detector, equipped with a spectrometer, makes measurements of the outgoing muon charge possible. Given that FASER $\nu$ 2 is based on the same detector technology as its predecessor, the same performance in terms of reconstruction of final-state kinematics can be assumed.

**AdvSND.** This proposed experiment [10] consists actually on two detectors, a far-detector to be installed at the FPF with a coverage in neutrino pseudorapidity of  $7.2 \leq \eta_\nu \leq 8.4$  (i.e., off-LOS, same as SND@LHC) and a near detector installed somewhere else in the LHC complex and covering the range  $4 \leq \eta_\nu \leq 5$ . Here we focus on the former. It would be composed (from upstream to downstream) by a target region for vertex reconstruction and electromagnetic energy measurement, followed by a hadronic calorimeter, a muon identification system, and finally a magnet enabling

muon charge and momentum measurements. The target region of the detector, where the neutrino interactions take place, is made of thin sensitive layers interleaved with tungsten plates, for a total mass of 5 tonnes and fiducial length of 50 cm. This detector configuration will be able to track muons with energy  $E_\nu \gtrsim 20 \text{ GeV}$  within an acceptance of 100 mrad and provide information on the charge of the outgoing muon thanks to its magnet. The total energy of the hadronic final state will be measured in the hadronic calorimeter. No information on the expected performance of the AdvSND-far detector is available and hence no estimate of the systematic errors is carried out.

**FLArE.** Building upon recent progress in liquid noble gas neutrino detectors over the last decade (ICARUS, MicroBooNE, SBND, DUNE), this experiment [10, 41] would rely on a modularized liquid argon (LAr) time projection detector. The use of LAr as a target is beneficial for final-state particle identification, track angle, and kinetic energy measurements with sub-millimeter spatial resolution in all dimensions. The detector will be equipped with a magnetized hadron/muon calorimeter downstream of the liquid argon volume for muon charge and momentum measure-

ments. While muon neutrinos with energy  $E_\nu \gtrsim 2$  GeV would not be fully contained in the FLArE detector, for our projections we assume that outgoing high-energy muons would be measured in the FASER2 spectrometer situated downstream in the FPF cavern.

With an expected fiducial (active) mass of 10 tonnes (30 tonnes) and a length of 7 m, FLArE will detect final-state electrons with energies  $E_e \lesssim 2$  TeV and scattering angles up to 0.5 mrad, while final-state muons with  $\theta_\mu \lesssim 0.025$  will be recorded by FASER2. Here we present projections for this baseline design of the experiment, FLArE10, as well as for a potential larger variant based on a fiducial mass of 100 tonnes, denoted FLArE100. While FLArE100 is not one of the currently proposed FPF experiments, we nevertheless include it for illustration purposes. Reconstruction of the total energy of the hadronic final state will be possible. In terms of performance, the targets are  $\delta E_\mu \sim 5\%$  of electron energy resolution,  $\delta\theta_e \sim 15$  mrad of electron angular resolution, and  $\delta E_h \sim 30\%$  for the hadronic energy. Since the muon energy from a charged-current interaction would be measured by FASER2, the performance parameters for  $E_\mu$  are taken to be the same.

### 2.3 Differential scattering event rates

For each of the LHC far-forward neutrino detectors described in Table 2.1, we generate projections for the expected DIS structure function measurements as follows. We want to evaluate the number of reconstructed charged-current neutrino interaction events taking place in the fiducial volume of the detector when divided into bins of Bjorken- $x$ , momentum transfer  $Q^2$ , and neutrino energy  $E_\nu$ , that is,

$$N_{\nu_e, \text{ev}}^{(i)}(\nu_e; E_\nu; x; Q^2), \quad i = 1, \dots, N_{\text{bin}}, \quad (2.11)$$

with

$$\begin{aligned} E_{\min}^{(i)} &\leq E_\nu \leq E_{\max}^{(i)}, \\ x_{\min}^{(i)} &\leq x \leq x_{\max}^{(i)}, \\ Q_{\min}^{2(i)} &\leq Q^2 \leq Q_{\max}^{2(i)}, \end{aligned}$$

for electron neutrinos and for each of the bins composing the measurement, and with similar expressions applying for muon neutrinos and antineutrinos. These event yields determine the statistical precision associated to a measurement of the double-differential cross-sections Eqns. (2.1) and (2.2). Subsequently, we account for the expected reconstruction performance of the detector in order to estimate the systematic uncertainties associated to these event yields. For simplicity, in this initial study we consider a single bin in energy and choose log-spaced bins in  $x$  and  $Q^2$ ; the eventual optimisation of the binning selection is left for future work.

In this calculation, we adopt the neutrino fluxes evaluated in [1] and used for the FPF simulations presented in [10]. The bin-by-bin integrated event yields in Eq. (2.11) are obtained by convoluting the incoming neutrino fluxes,

for a given acceptance of the target detector, with the corresponding neutrino differential cross-sections Eqns. (2.1) and (2.2). Binned event yields are evaluated using

$$\begin{aligned} N_{\text{ev}}^{(i)} = &n_T L_T \int_{Q_{\min}^{2(i)}}^{Q_{\max}^{2(i)}} \int_{x_{\min}^{(i)}}^{x_{\max}^{(i)}} \int_{E_{\min}^{(i)}}^{E_{\max}^{(i)}} \frac{dN_\nu(E_\nu)}{dE_\nu} \\ &\left( \frac{d^2\sigma(x, Q^2, E_\nu)}{dx dQ^2} \right) \mathcal{A}(x, Q^2, E_\nu) dQ^2 dx dE_\nu, \end{aligned} \quad (2.12)$$

with  $n_T$  is the nucleon density of the target detector material,  $L_T$  its length, and  $\mathcal{A}(x, Q^2, E_\nu)$  is a global acceptance factor which takes the form of a step function and accounts for the experimental acceptances in  $E_\ell$ ,  $\theta_\ell$ , and  $E_h$  listed in Table 2.1.

The incoming neutrino fluxes of [1] account for the geometry and neutrino pseudo-rapidity  $\eta_\nu$  coverage of the considered detector and are encoded in Eq. (2.12) as  $dN_\nu(E_\nu)/dE_\nu$ . This neutrino flux takes into account both the prompt component associated with neutrinos from charmed hadron decay as well as a displaced component from light hadron decays. The prompt component used in this work was simulated at NLO using POWHEG [64–66] matched to PYTHIA8 [67, 68] for the parton shower and hadronisation, and the displaced component was simulated with EPOS-LHC [69]. In comparison with the calculation from [1], in addition to the improved charmed hadron production presented in [70], the neutrino flux has been updated to  $\sqrt{s} = 13.6$  TeV.

As pointed out in Ref. [1] there are notable neutrino flux uncertainties, as various event generators do not agree on the forward parent hadron spectra. The spread of the generators' predictions can be taken as a means of flux uncertainty, in which case there is a  $\lesssim 50\%$  uncertainty on the interacting muon neutrino spectrum — if left unresolved this would be a significant systematic. Indeed, there are already projections of FPF measurements which would reduce this uncertainty [71] as well as efforts to describe the uncertainty in a data-driven way while improving the modelling of forward hadronization [72]. However, it is important to note that forward neutrino experiments actually constrain the product of flux and cross-section, and one must be assumed to measure the other. In a full analysis, they would be constrained simultaneously in a joint measurement. In our study, we aim to understand the full impact of FPF data on the PDF fit, thus motivating this future joint measurement. To this aim, we take the neutrino flux to be known and focus on the irreducible systematics associated with event reconstruction.

The triple integral in Eq. (2.12) is evaluated numerically by means of Monte Carlo sampling, by generating  $N_{\text{mc}}$  sampling points in the  $(x, Q^2, E_\nu)$  space with the constraint that

$$0 < y (= Q^2/2m_N E_\nu x) < 1, \quad (2.13)$$

and where  $N_{\text{mc}}$  is chosen to be large enough such that residual Monte Carlo integration uncertainties are negligible for all the bins considered.

Eq. (2.12) can be generalised to charm-production events, with the only difference being that now the neu-

trino scattering cross-section is restricted to those processes leading to final-state charm quarks. Assuming that charm quarks can be directly tagged by the detector one has

$$N_{\text{ev},c}^{(i)} = n_T L_T \int_{Q_{\min}^{(i)}}^{Q_{\max}^{(i)}} \int_{x_{\min}^{(i)}}^{x_{\max}^{(i)}} \int_{E_{\min}^{(i)}}^{E_{\max}^{(i)}} \frac{dN_\nu(E_\nu)}{dE_\nu} \quad (2.14)$$

$$\left( \frac{d^2\sigma^{\nu N \rightarrow \ell + c + X}(x, Q^2, E_\nu)}{dx dQ^2} \right) \mathcal{A}(x, Q^2, E_\nu) dQ^2 dx dE_\nu,$$

with the charm production cross-sections discussed in [21] and references therein. Here we neglect efficiency and acceptance effects associated to  $D$ -meson tagging, which can only be properly estimated by means of a full detector simulation. The acceptance correction  $\mathcal{A}(x, Q^2, E_\nu)$  in Eq. (2.14) applies only to the charged leptons and hence is the same as in the inclusive case.

Detectors without charm-tagging capabilities can still be sensitive to charm production via the semileptonic decays of the  $D$ -mesons, resulting in the characteristic dimuon topology, where

$$N_{\text{ev},2\mu}^{(i)} \approx N_{\text{ev},c}^{(i)} \times \mathcal{B}(c \rightarrow D \rightarrow \mu + X), \quad (2.15)$$

with  $\mathcal{B}$  a numerical factor that accounts for charm hadronisation and the resulting semileptonic decay to a muon. Given that  $\mathcal{B} \sim 0.1$ , being able to tag directly charm quarks increases the event yields of charm production events by a factor of 10 as compared to reconstructing the dimuon final state.

Table 2.2 summarises the predicted integrated event yields for the detectors considered, separated into electron neutrinos and antineutrinos and muon neutrinos and antineutrinos. We used the PDF4LHC21 set to compute the differential cross sections that enter in Eq. 2.12. As mentioned above, for FLArE we assume that muon neutrinos interacting in its fiducial volume will be measured by the FASER $\nu$ 2 spectrometer. These event yields are computed from Eq. (2.12) with the requirement that the momentum transfer and the final-state invariant mass are restricted to the DIS region,

$$Q^2 \geq 2 \text{ GeV}^2 \quad \text{and} \quad W^2 \geq 4 \text{ GeV}^2. \quad (2.16)$$

The numbers in parenthesis indicate the event rates corresponding to charm production, assuming heavy flavour tagging capabilities. In the case of the FLArE detector, we display results for two proposed options with fiducial masses of 10 and 100 tonnes. As opposed to the number of interacting neutrinos presented in [10], we now account for the detector acceptances listed in Table 2.1, which reduce the event yields by up to a factor 2.

Several observations can be derived from Table 2.2. First, one appreciates the large increase in statistics from the Run III experiments to the FPF ones, with for example a factor of  $\sim 250$  increase in the muon neutrino yield between FASER $\nu$  and FASER $\nu$ 2. Second, the muon-neutrino scattering yield dominates over electron neutrino scattering by a factor between 2 and 3, though the precise value of this ratio is affected by the large theory uncertainties affecting forward electron neutrino production. Third,

charm production represents around 15% of the inclusive yields, with both FASER $\nu$ 2 and FLArE100 resulting in around 80k recorded charm-production events. Note that this result assumes  $D$ -meson tagging capabilities, and if only dimuon events can be recorded the yields would be reduced by a factor of 10. Fourth, FASER $\nu$ 2 and FLArE100 lead to the largest absolute yields of the FPF experiments, with a total of around 680k and 1.1M (non-tau) neutrino DIS events respectively, with 74k and 170k events expected instead for AdvSND-far and for FLArE10.

Fig. 2.1 displays the differential event yields per bin, Eq. (2.11), for muon neutrinos detected at the FASER $\nu$  (Run III) and the AdvSND, FASER $\nu$ 2, and FLArE100 (FPF) experiments, restricted to the DIS region defined by Eq. (2.16) and where only bins with  $\geq 100$  events are retained, except for FASER $\nu$  in which bins with  $\geq 10$  events are shown. Adding up the bins in each of the panels results into the inclusive yields listed in Table 2.2. The clear improvement in going from the current FASER $\nu$  experiment to the FPF ones is visible both in terms of the number of events per bin as well as for the kinematic coverage. The FPF experiments benefit from large event rates for most of the region in  $(x, Q^2)$  covered, leading to typical statistical uncertainties at the 1% level or smaller, while for FASER $\nu$  the statistical uncertainties are larger due to the reduced event rates.

From Fig. 2.1 one observes how the kinematic coverage of the FPF far-forward experiments reaches down to  $x_{\min} \sim 3 \times 10^{-3}$  at small- $x$  and up to  $Q_{\max}^2 \sim 10^4 \text{ GeV}^2$  at large- $Q^2$ , representing an extension of around one order of magnitude in both directions as compared to available DIS neutrino data. To illustrate this, Fig. 2.2 compares the kinematic coverage of FASER $\nu$ , FASER $\nu$ 2, FLArE, and AdvSND, same as in Fig. 2.1, with that of electron-ion collisions at the upcoming EIC [35, 36] at the highest centre-of-mass energies planned, as well as to available fixed-target neutral- and charged-current DIS measurements. The LHC neutrino experiments cover an  $x$  region relevant at hadron colliders for Higgs boson analyses, precision electroweak measurements such as the  $W$ -boson mass [73], and new physics measurements sensitive to the large- $x$  PDFs [74]. FASER $\nu$ 2 and FLArE100 mostly overlap with the EIC coverage, providing a complementary handle on the quark flavour decomposition in protons and heavy nuclei as compared to the one provided by the EIC measurements.

The inclusive yields listed in Table 2.2 differ from the total number of neutrinos interacting within the detector volume [1, 10] due to both the DIS requirements ( $W^2 > 4 \text{ GeV}^2$  and  $Q^2 > 2 \text{ GeV}^2$ ) and the detector fiducial acceptances summarised in Table 2.1. The former is found to be negligible, with DIS cuts removing only  $\lesssim 1\%$  of the events, a consequence of the high energy of LHC neutrinos. The latter is quantified in Table 2.3, displaying the total number of electron and muon neutrinos before and after applying acceptance cuts. The acceptance efficiency, defined as the ratio between pre- and post-acceptance integrated event yields, depends on the detector and can be up to 50%. For instance, FASER $\nu$ 2 loses 63% and 52% of the

Detector	$N_{\nu_e}$	$N_{\bar{\nu}_e}$	$N_{\nu_e} + N_{\bar{\nu}_e}$	$N_{\nu_\mu}$	$N_{\bar{\nu}_\mu}$	$N_{\nu_\mu} + N_{\bar{\nu}_\mu}$
FASER $\nu$	400 (62)	210 (38)	610 (100)	1.3k (200)	500 (90)	1.8k (290)
SND@LHC	180 (22)	76 (11)	260 (32)	510 (59)	190 (25)	700 (83)
FASER $\nu 2$	116k (17k)	56k (9.9k)	170k (27k)	380k (53k)	133k (23k)	510k (76k)
AdvSND-far	12k (1.5k)	5.5k (0.82k)	18k (2.3k)	40k (4.8k)	16k (2.2k)	56k (7k)
FLArE10	44k (5.5k)	20k (3.0k)	64k (8.5k)	76k (10k)	38k (5.0k)	110k (15k)
FLArE100	290k (35k)	130k (19k)	420k (54k)	440k (60k)	232k (30k)	670k (90k)

**Table 2.2.** Integrated event yields for the six detectors considered, separated into electron neutrinos and antineutrinos, muon neutrinos and antineutrinos, and their sum. These event yields are computed from Eq. (2.12) imposing DIS kinematics,  $Q^2 \geq 2$  GeV $^2$  and  $W^2 \geq 4$  GeV $^2$ . The numbers in parenthesis indicate the event rates corresponding to charm production, Eq. (2.14). In the case of the FLArE detector, we display results for two proposed options with fiducial masses of 10 and 100 tonnes respectively.

Detector	before cuts	after DIS and acceptance cuts	acceptance efficiency
	$N_{\nu_e} + N_{\bar{\nu}_e}, N_{\nu_\mu} + N_{\bar{\nu}_\mu}$	$N_{\nu_e} + N_{\bar{\nu}_e}, N_{\nu_\mu} + N_{\bar{\nu}_\mu}$	$N_{\nu_e} + N_{\bar{\nu}_e}, N_{\nu_\mu} + N_{\bar{\nu}_\mu}$
FASER $\nu$	1.2k, 4.1k	610, 1.8k	51%, 44%
SND@LHC	280, 860	260, 700	92%, 81%
FASER $\nu 2$	270k, 980k	170k, 510k	63%, 52%
AdvSND-far	19k, 66k	18k, 56k	95%, 85%
FLArE10	65k, 202k	64k, 110k	98%, 55%
FLArE100	427k, 1.3M	420k, 670k	98%, 52%

**Table 2.3.** The number of electron and muon neutrinos interacting within the detector volume, compared with the results after applying the DIS requirements ( $W^2 > 4$  GeV $^2$  and  $Q^2 > 2$  GeV $^2$ ) and the experimental acceptances from Table 2.1. The DIS requirement removes only  $\lesssim 1\%$  of the events, a consequence of the high energy of LHC neutrinos. The last column displays the acceptance efficiency, defined as the ratio between pre- and post-acceptance integrated event yields. While the specific efficiencies depend on the experiment, up to 50% of the neutrinos interacting in the detector volume may fall outside detector acceptance.

interacting electron and muon neutrinos respectively due to the acceptance requirements. From Table 2.1, is it also worth noting how FLArE has virtually perfect acceptance for electron neutrinos. One also observes that SND@LHC and AdvSND exhibit relatively large acceptance efficiencies, which however are not sufficient to compensate for the lower number of initial interacting neutrinos due to their off-axis location as compared to FASER $\nu(2)$  and FLArE.

#### 2.4 Statistical and systematic uncertainties

The event yields displayed in Fig. 2.1 determine the associated statistical uncertainty in each bin,

$$\delta^{(\text{stat})} N_{\text{ev}}^{(i)} = \sqrt{N_{\text{ev}}^{(i)}}, \quad (2.17)$$

such that the fractional statistical uncertainty per bin is  $\delta_i^{(\text{stat})} = 1/\sqrt{N_{\text{ev}}^{(i)}}$ . Since we discard bins with less than 100 events for FPF experiments (FASER $\nu 2$ , FLArE, AdvSND) and 10 events for FASER $\nu$  and SND@LHC, the fractional statistical uncertainty ranges between  $\lesssim 1\%$  and  $\sim 30\%$ , depending on the values of  $x$  and  $Q^2$  associated to each bin.

The projected statistical uncertainties for muon-neutrino scattering in the case of FASER $\nu 2$  are displayed in the left panel of Fig. 2.3, which corresponds to the same event yields as in Fig. 2.1 for now as a function of  $x$  after having integrated the event yields in the range  $Q^2 \in [10, 100]$  GeV $^2$ . The error bar in the vertical direction indicates the statistical uncertainties, while that in the horizontal direction corresponds to the width of the  $x$ -bins. Except

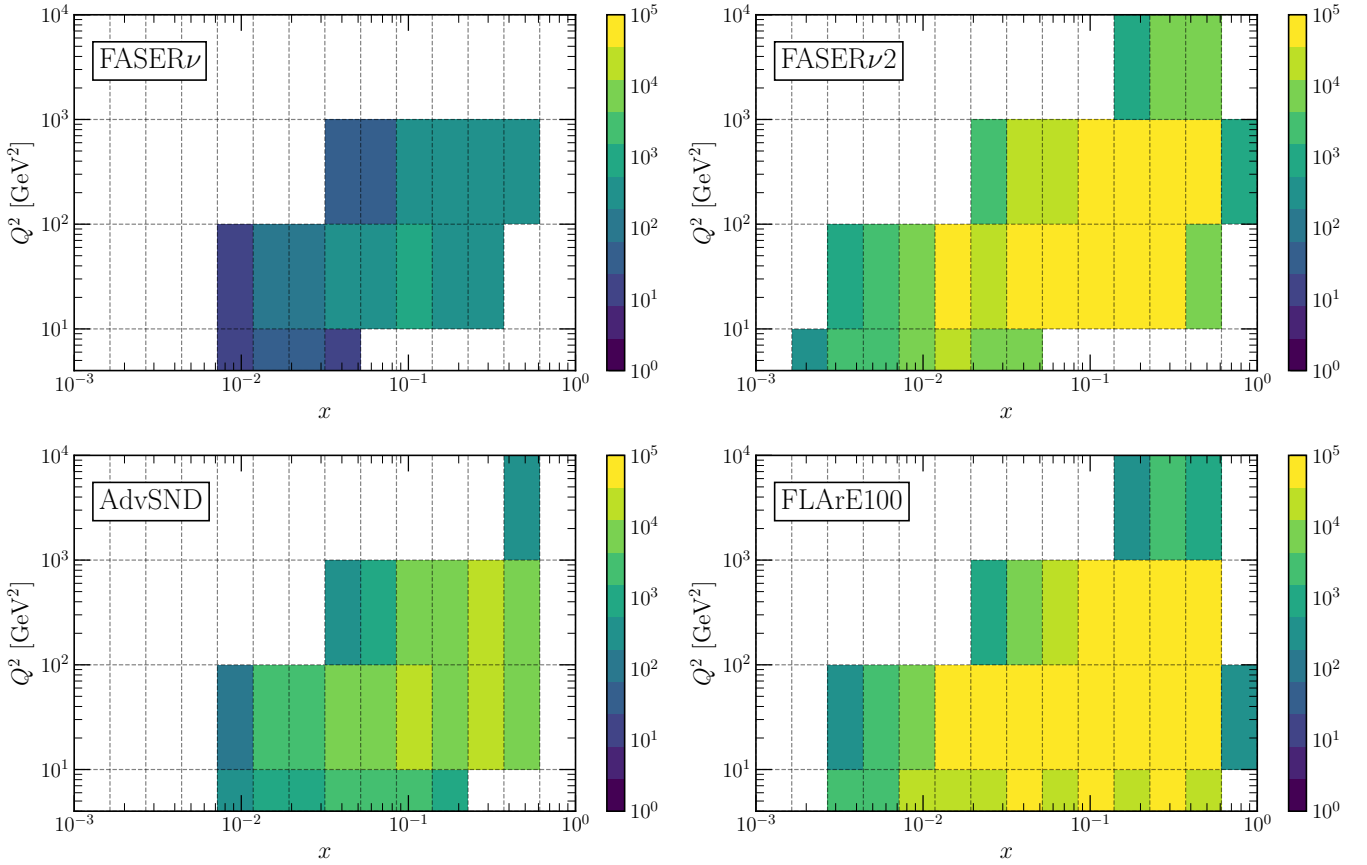


**Fig. 2.1.** The event yields per bin  $N_{\text{ev}}^{(i)}$ , Eq. (2.11), for muon-neutrino scattering at the FASER $\nu$ , FASER $\nu$ 2, AdvSND, and FLArE100 experiments. Selected events are restricted to the DIS region Eq. (2.16) and only bins with  $\geq 100$  events are retained except for FASER $\nu$  in which bins with  $\geq 10$  events are kept. Adding up the bins in each of the panels results into the numbers listed in Table 2.2.

for the bins with the smallest values of  $x$ , statistical uncertainties indeed are at the percent level or smaller for this experiment.

In addition to the statistical uncertainties evaluated from Eq. (2.17), one needs to also estimate the systematic uncertainties associated to the finite precision in the reconstruction of the final state leptonic and hadronic variables listed in Table 2.1. For instance, an event which would be classified into a given bin in  $(x, Q^2, E_\nu)$  in the case of a perfect detector may end up being mis-classified into a different bin in the presence of systematic shifts associated to the lepton energy  $E_\ell$ , lepton scattering angle  $\theta_\ell$ , and hadronic energy  $E_h$ , as indicated by Eq. (2.10).

For each independent source of systematic uncertainty, which in this analysis consists of  $\delta E_\ell$ ,  $\delta E_h$ , and  $\delta \theta_\ell$ , we quantify its impact at the event yield level

$$\delta_{\text{sys}}^{(E_\ell)} N_{\text{ev}}^{(i)}, \quad \delta_{\text{sys}}^{(E_h)} N_{\text{ev}}^{(i)}, \quad \delta_{\text{sys}}^{(\theta_\ell)} N_{\text{ev}}^{(i)}, \quad i = 1, \dots, N_{\text{bin}}, \quad (2.18)$$

by extending the calculation delineated in Sect. (2.3). First, we generate a Monte Carlo set of events, denoted by  $\mathcal{D}_0$ , composed by  $N_{\text{mc}} \approx 10^7$  samples and determine the assignment of each event to a point in the  $(x, Q^2, E_\nu)$  space. We then take each event in  $\mathcal{D}_0$  and smear it with Gaussian

distributions whose variances are given by Table 2.1 to produce a set of new samples  $\{\mathcal{D}_k\}$ . The smeared events are subjected to the same DIS cuts from Eq. (2.16) and acceptances from Table 2.1. The bin assignment of the events in the smeared samples  $\mathcal{D}_k$  will in general be different from those of the baseline sample  $\mathcal{D}_0$ .

We define the fractional uncertainty associated to a given systematic source, say  $\delta E_\ell$ , for bin  $i$  to be the mean of the absolute difference between the number of events in this bin for the smeared samples  $\{\mathcal{D}_k\}$  and the number of events in this bin for  $\mathcal{D}_0$ :

$$\delta_{\text{sys}}^{(E_\ell)} = \left\langle \left| \frac{N_{E_\ell-\text{smeared},k}^{(i)} - N_0^{(i)}}{N_0^{(i)}} \right| \right\rangle. \quad (2.19)$$

The absolute systematic uncertainty in event yield caused by  $\delta E_\ell$  is then  $\delta_{\text{sys}}^{(E_\ell)} N_{\text{ev}}^{(i)}$ . Individual sources of systematic errors are treated as uncorrelated among them, and hence by producing samples where only one source of error is varied at a time we can determine the systematic errors, Eq. (2.18), in each bin for each of the considered experiments. This approach has the benefit that rescaling individual sources of systematic uncertainties, say to assess

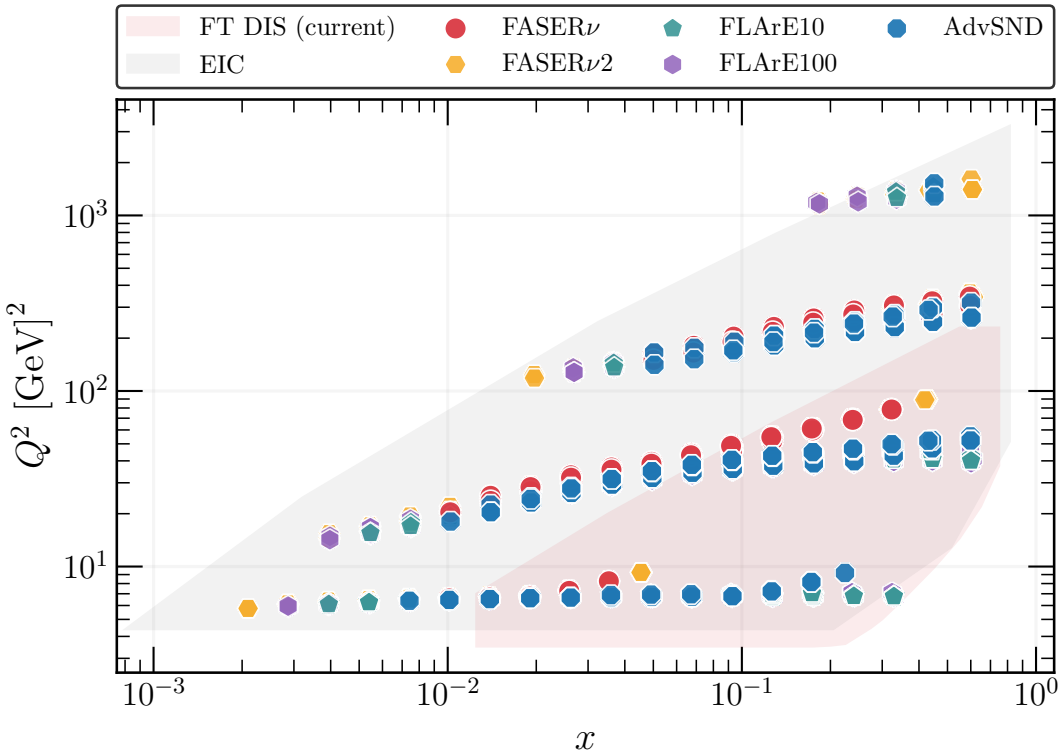


**Fig. 2.2.** The kinematic coverage in the  $(x, Q^2)$  plane of muon-neutrino scattering at the FASER $\nu$ , FASER $\nu$ 2, FLArE10(100), and AdvSND experiments, see also Fig. 2.1, compared to that of electron-ion collisions at the EIC as well as to the coverage of existing neutrino fixed-target DIS measurements.

the impact of improved detector performance, becomes straightforward.

Fig. 2.4 displays the projected systematic uncertainties associated to  $E_\ell$ ,  $\theta_\ell$ , and  $E_h$  for the measurements of the double-differential muon-neutrino scattering at FASER $\nu$ 2. We note that there is a further systematic uncertainty associated to the overall neutrino flux, but we do not include this uncertainty in our estimation. The magnitude of each systematic error is plotted as a function of the average momentum fraction per bin  $\langle x \rangle$  in two different bins of  $Q^2$ . We indicate separately the results for neutrino and antineutrino projectiles as well as those associated to inclusive and to charm production measurements. For completeness, we also display in the bottom-right panel the corresponding statistical uncertainties in the same bins.

In the case of FASER $\nu$ 2, the systematic uncertainties associated to the final state energies  $E_\ell$  and  $E_h$  are comparable and are in general at the 10% level, ranging from 1% to 30% across bins. The uncertainties associated with  $\theta_\ell$  are typically at or well below the 1% level for these experiments, which can be attributed to their good spatial resolution. On the other hand, for the FLArE experiment, uncertainties associated with the scattering angle  $\theta_\ell$  dominate, being at the 40% level and ranging from a few percent to  $\mathcal{O}(1)$ , whereas the uncertainties associated with final-state energy reconstruction are smaller, around the 10% level, and range from  $\lesssim 1\%$  to up to around 80% depending

on the bin. For all experiments, statistical uncertainties are subdominant in most of the bins and are below the 10% level, especially at large- $x$  which is the kinematic region benefitting from the largest event rates.

Fig. 2.3 also displays the integrated event yields for FASER $\nu$ 2 as a function of  $x$  for only systematic errors and for the sum in quadrature of statistical and systematic errors (central and right panels respectively). For most of the bins, for the baseline performance assumptions the total systematic uncertainty dominates over the statistical uncertainties, with the possible exception of the small- $x$  region where statistical and systematic errors are of comparable size.

The end result of the procedure is an estimate of the statistical and systematic uncertainties for each bin of the measurement, from which an experimental covariance matrix can be constructed as

$$\text{cov}_{ij} = \delta_{ij} \left( \delta^{(\text{stat})} N_{\text{ev}}^{(i)} \right)^2 + \sum_{k=1}^{n_{\text{sys}}} \left( \delta_{\text{sys}}^{(k)} N_{\text{ev}}^{(i)} \right) \left( \delta_{\text{sys}}^{(k)} N_{\text{ev}}^{(j)} \right),$$

for  $i, j = 1, \dots, N_{\text{bin}}$ , (2.20)

and the same for the associated correlation matrix of the measurement

$$\rho_{ij} = \frac{\text{cov}_{ij}}{\sqrt{\text{cov}_{ii}} \sqrt{\text{cov}_{jj}}}. \quad (2.21)$$

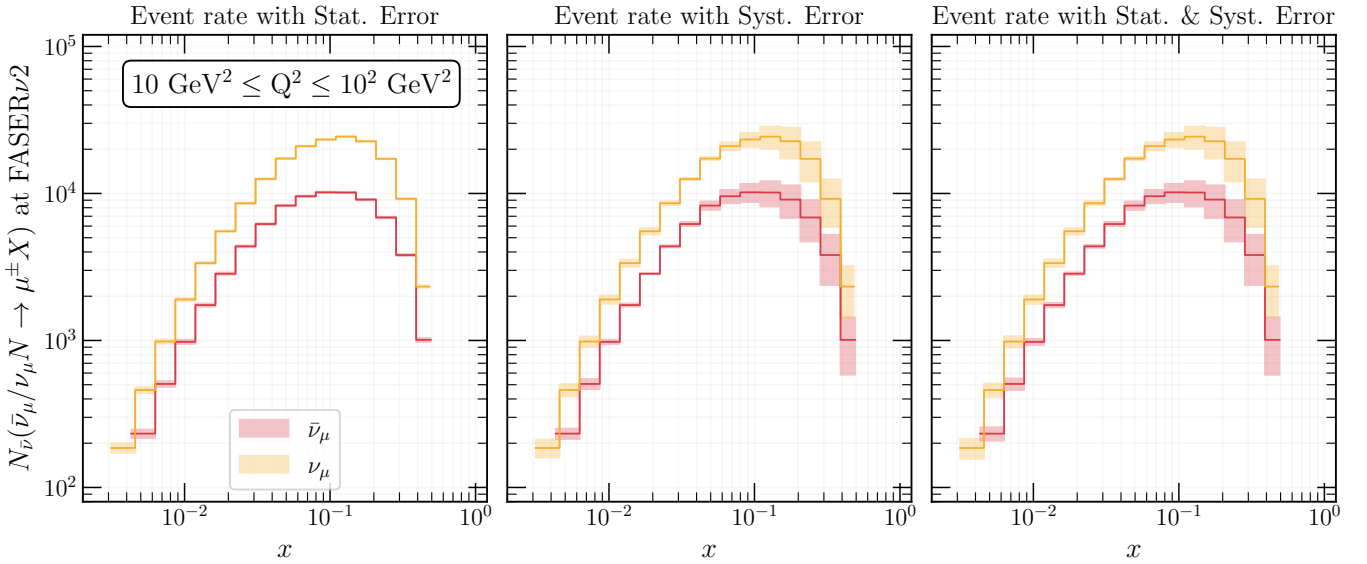


**Fig. 2.3.** Same as Fig. 2.1 for FASER $\nu_2$  now as a function of  $x$  after having integrated the event yields in the range  $Q^2 \in [10, 100]$   $\text{GeV}^2$  for both the neutrino and antineutrinos. In addition to the event yield values, we also show the error bars corresponding to statistical errors only (left), systematic errors only (middle), and the sum in quadrature of the two (right panel). The bars in the horizontal direction indicate the width of the adopted  $x$ -bins.

The relative covariance matrix,  $\text{cov}_{ij}/(N_{\text{ev}}^{(i)} N_{\text{ev}}^{(j)})$ , is independent of the considered observable and would also apply for the double-differential cross-sections Eqns. (2.1) and (2.2) which are related to the event yields by a constant prefactor.

The experimental covariance matrix constructed as per Eq. (2.20) assumes that each source of systematic uncertainty is 100% correlated across all the bins of the measurement. In the real experiment, the actual covariance matrix will be composed by a large number of uncertainty sources, with typical HERA and LHC precision measurements characterised by up to hundreds of different sources of systematic error. In particular, the assumption that a single source of systematic error, say  $\delta E_\ell$ , is fully correlated among all the bins in  $(x, Q^2)$  is unlikely to be accurate.

For this reason, following the HL-LHC projection strategy of [34], here we neglect bin-by-bin correlations and add in quadrature statistical and systematic errors,

$$\text{cov}_{ij} = \delta_{ij} \left( \delta^{(\text{stat})} N_{\text{ev}}^{(i)} \right)^2 + \delta_{ij} (f_{\text{corr}})^2 \sum_{k=1}^{n_{\text{sys}}} \left( f_{\text{red}}^{(k)} \right)^2 \times \left( \delta_{\text{sys}}^{(k)} N_{\text{ev}}^{(i)} \right)^2 \quad \text{for } i, j = 1, \dots, N_{\text{bin}}. \quad (2.22)$$

In Eq. (2.22) we have introduced a parameter  $f_{\text{red}}^{(k)} \leq 1$  that gauges the impact of a possible reduction of the  $k$ -th systematic error as compared to the default experiment performance (reproduced with  $f_{\text{red}} = 1$ ). Furthermore,  $f_{\text{corr}}$  represents an effective correction factor that accounts for the fact that data with correlated systematics may be more constraining than the same data where each source of error is simply added in quadrature as we do here. A value of  $f_{\text{corr}} \sim 0.5$ , obtained from the inspection of available

measurements for which the full information on correlated systematics is available, was estimated in [34] and we adopt the same choice here.

In Sect. 3 we present results both for  $f_{\text{red}} = 1$  (conservative) and  $f_{\text{red}} = 0.5$  (optimistic scenario), though we note that it would be straightforward to revisit the projections for other assumptions of the detector performance. Specifically,  $f_{\text{red}} = 0.5$  is assumed for the Hessian profiling of PDF4LHC21 and EPPS21 while  $f_{\text{red}} = 1$  for the NNPDF4.0-based fits.

## 2.5 Pseudo-data generation

In order to generate pseudo-data for double-differential LHC neutrino scattering cross-sections, we follow the procedure used for the HL-LHC projections of [34] which was also adopted in [75] and [76] for SMEFT impact projections of vector-boson scattering and high-mass Drell-Yan data at the HL-LHC, respectively. The starting point are predictions for inclusive and charm-tagged differential neutrino scattering cross-section, denoted generically by

$$\mathcal{O}_i^{(\text{th})} \equiv \frac{d^2 \sigma^{\nu N}(x_i, Q_i^2, y_i)}{dx dy}, \quad i = 1, \dots, N_{\text{bin}}, \quad (2.23)$$

with  $(x_i, Q_i^2, y_i)$  labeling the corresponding bin centres. The observables  $\mathcal{O}_i$  in Eq. (2.23) are evaluated with YADISM [15, 54] interfaced to PINEAPPL [55, 77] to return a fast interpolation grid admitting a generic PDF input, and with DGLAP evolution effects provided by EKO [53]. DIS structure functions are evaluated at NNLO in the QCD expansion and account both for heavy quark and target mass

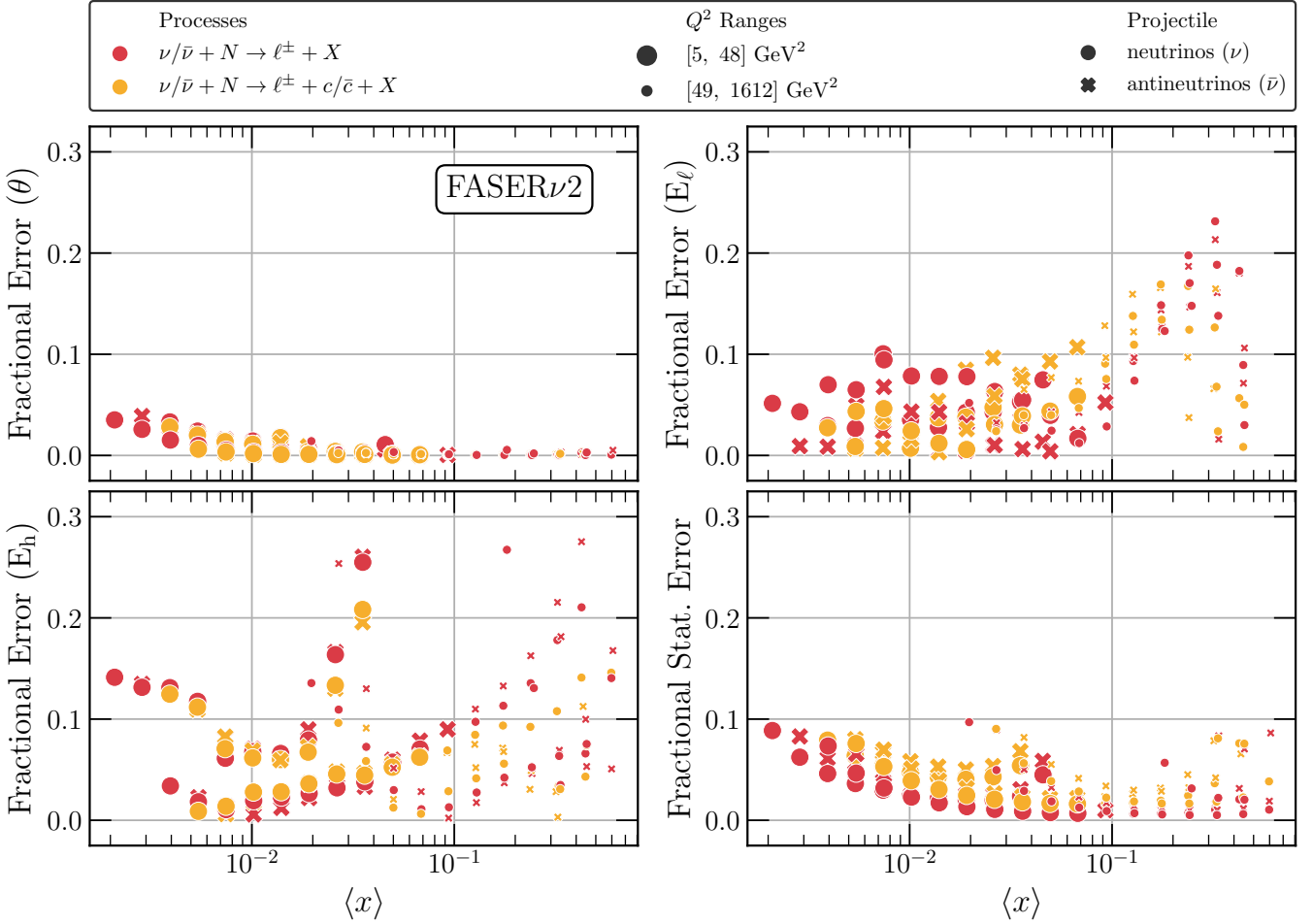


**Fig. 2.4.** Estimated systematic uncertainties for the measurements of the double-differential muon-neutrino scattering cross-section at FASER $\nu$ 2. We consider the systematic errors associated to the charged-lepton energy  $E_\ell$  and scattering angle  $\theta_\ell$  and to the hadronic energy  $E_h$ . The size of each source of systematic error is plotted as a function of the average momentum fraction per bin  $\langle x \rangle$  in two different bins of  $Q^2$ . We indicate separately the results for neutrino and antineutrino projectiles as well as those associated to inclusive and to charm production measurements. For completeness, we display in the bottom-right panel the corresponding statistical uncertainties in the same bins.

effects. No higher-twists corrections are included. In particular, charm structure functions are evaluated in the FONLL general-mass variable-flavour-number scheme [21, 78, 79] at  $\mathcal{O}(\alpha_s)$  accuracy. For the proton PDF fits, we assume a free isoscalar target  $N$ , while for the nuclear PDF one we allow for deviations from isoscalarity relevant for a tungsten nucleus.

To ensure consistency, the PDF set and other theory settings, such as the perturbative order and heavy quark scheme, adopted for the evaluation of Eq. (2.23) should be the same as those used in the fitting framework assessing their impact. For instance, when using the xFITTER profiling of PDF4LHC21, one needs to generate neutrino structure functions also using PDF4LHC21 as input. This ensures that the generated pseudo-data is coherent with the prior PDF set used as baseline and avoids introducing artificial inconsistencies compromising the validity of the projection studies.

The central values for the pseudo-data, denoted by  $\mathcal{O}_i^{(\text{exp})}$ , are obtained by fluctuating the reference theory prediction Eq. (2.23) by the corresponding fractional statistical and systematic uncertainties,

$$\mathcal{O}_i^{(\text{exp})} = \mathcal{O}_i^{(\text{th})} (1 + r_i \delta_i^{\text{tot}}), \quad i = 1, \dots, N_{\text{bin}}, \quad (2.24)$$

where the total experimental uncertainty is the sum in quadrature of statistical and systematic errors, accounting for a possible reduction factor in the latter,

$$\delta_i^{\text{tot}} = \left( (\delta_i^{\text{stat}})^2 + \sum_{k=1}^{n_{\text{sys}}} \left( f_{\text{corr}} \times f_{\text{red}}^{(k)} \times \delta_{i,k}^{\text{sys}} \right)^2 \right)^{1/2},$$

for  $i = 1, \dots, N_{\text{bin}}$ ,

(2.25)

and with  $r_i$  being univariate Gaussian random numbers. As mentioned above,  $f_{\text{red}}^{(k)}$  is a reduction factor modelling

improvements in the experimental performance as compared to the baseline settings summarised in Sect. 2.1. The pseudo-data generated by means of Eq. (2.24), together with the corresponding covariance matrix computed according to Eq. (2.22), define then the inputs of the subsequent proton and nuclear PDF determinations.

## 2.6 PDF impact assessment

We consider two complementary approaches to assess the impact of the projected LHC neutrino data on the proton and nuclear PDFs. First, the Hessian profiling [34, 43–45] of prior proton and nuclear PDF sets, taken to be PDF4LHC21 [46] and EPPS21 [31] respectively. Second, the direct inclusion in the NNPDF global analysis framework [28, 51].

The profiling method applied to Hessian PDF fits is based on minimising a goodness-of-fit error function defined as

$$\chi^2 = \sum_{i=1}^{N_{\text{bin}}} \frac{\left( \mathcal{O}_i^{(\text{exp})} + \Gamma_i^{\alpha, \text{exp}} b_\alpha^{(\text{exp})} - \mathcal{O}_i^{(\text{th})} - \Gamma_i^{\beta, \text{th}} b_\beta^{(\text{th})} \right)^2}{\left( \delta^{(\text{stat})} \mathcal{O}_i^{(\text{th})} \right)^2} + \sum_{\alpha} \left( b_\alpha^{(\text{exp})} \right)^2 + T^2 \sum_{\beta} \left( b_\beta^{(\text{th})} \right)^2, \quad (2.26)$$

with the pseudodata  $\mathcal{O}_i^{(\text{exp})}$  defined in Eq. (2.24). The correlated uncertainties for the pseudodata and for the theoretical prediction are contained in the nuisance parameter vectors  $b^{(\text{exp})}$  and  $b^{(\text{th})}$ , respectively, with  $T$  the tolerance factor, and the total uncorrelated uncertainty is  $\delta^{(\text{stat})} \mathcal{O}_i^{(\text{th})}$ .

The effect of the nuisance parameters on the observables  $\mathcal{O}_i^{(\text{exp})}$  and  $\mathcal{O}_i^{(\text{th})}$  is described by the matrices  $\Gamma_i^{\text{exp}}$  and  $\Gamma_i^{\text{th}}$ . The indices  $\alpha$  and  $\beta$  then run over the uncertainty nuisance parameters for the pseudodata and the theoretical prediction, respectively. The nuisance parameter values  $b_\beta^{(\text{th}, \text{min})}$  that minimize Eq. (2.26) give the central PDFs  $f'_0$  optimized to the profiled dataset in the form

$$f'_0 = f_0 + \sum_{\beta} b_\beta^{(\text{th}, \text{min})} \left( \frac{f_{\beta}^{+} - f_{\beta}^{-}}{2} - b_\beta^{(\text{th}, \text{min})} \frac{f_{\beta}^{+} + f_{\beta}^{-} - 2f_0}{2} \right) \quad (2.27)$$

where  $f_0$  is the original central PDF and the up and down variation eigenvectors are given by  $f^+, f^-$ . The reduction in the uncertainties of the profiled PDFs indicate the impact of the projected data with respect to the assumed prior PDF set.

The profiling studies carried out in this work are performed using version 2.2.1 of the xFITTER open-source QCD analysis framework [47–50]. To this end, a new interface between PINEAPPL and xFITTER has been developed and is made available in xFITTER. All the experimental and theoretical data files used in the analysis, including the PINEAPPL grids, are available from the public xFITTER repository. For the proton PDF profiling, a

tolerance of  $T^2 = 10$  is adopted, which corresponds approximately to the average tolerance used in the CT18 [29] and MSHT20 [30] determinations, the two Hessian sets entering the PDF4LHC21 combination [46], for one-sigma PDF uncertainties. For the Hessian profiling of EPPS21, a value of  $T^2 = 33$  is used consistently with [31], and the resulting uncertainties are scaled down by a factor of 1.645 to obtain 68% confidence level intervals.

Concerning the inclusion of the LHC neutrino pseudo-data in the NNPDF proton analysis framework, we follow the procedure outlined in [51]. Fast interpolation tables (FK-tables) [80] combining EKO DGLAP evolution with YADISM DIS coefficient functions are computed using PINEAPPL, see also [81]. Predictions for the fitted observables Eq. (2.23) are evaluated with NNPDF4.0 NNLO and included in the corresponding PDF determination alongside all other datasets already present in the global fit. We verify that in all cases  $\chi^2/n_{\text{dat}} \sim 1$  after the fit, as expected given the built-in consistency between the prior PDF fit and the generated pseudo-data.

## 3 Constraints on proton and nuclear structure

By following the strategy outlined in Sect. 2, we quantify the impact on the proton and nuclear PDFs of differential DIS cross-section measurements obtained with the LHC neutrino beam. Here we present results first for the Hessian profiling of the PDF4LHC21, then for the Monte Carlo fit NNPDF4.0, and finally for the nuclear PDFs of EPPS21, also by means of profiling. We study the stability of the results with respect to the inclusion of systematic uncertainties, charm-tagged data, and lepton-charge separation. We also compare the impact of the different FPF experiments separately and provide results for their combination. For completeness, we study in App. A the constraints on PDFs provided by the forward experiments, namely FASER $\nu$ . The results show that measurements at FASER $\nu$  are unable to improve the determination of PDFs therefore strengthening the need for the FPF experiments.

### 3.1 Proton PDFs: impact on PDF4LHC21

We begin with the Hessian profiling of the PDF4LHC21 set. This proton PDF set is a Monte Carlo combination [82, 83] of three global PDF sets, CT18 [29], MSHT20 [30], and NNPDF3.1 [84]. Its Hessian representations are obtained by means of the reduction methodologies developed in [85–87]. Being based on the combination of three modern global PDF fits, PDF4LHC21 provides a conservative estimate of current uncertainties associated to our understanding of proton PDFs. We profile PDF4LHC21 with pseudodata from various LHC neutrino experiments, and study the stability of the results with respect to variations in the profiling inputs.

**Constraints from FASER $\nu$ 2.** Fig. 3.1 shows the fractional uncertainties (at the 68% confidence level) at  $Q^2 = 10^4 \text{ GeV}^2$

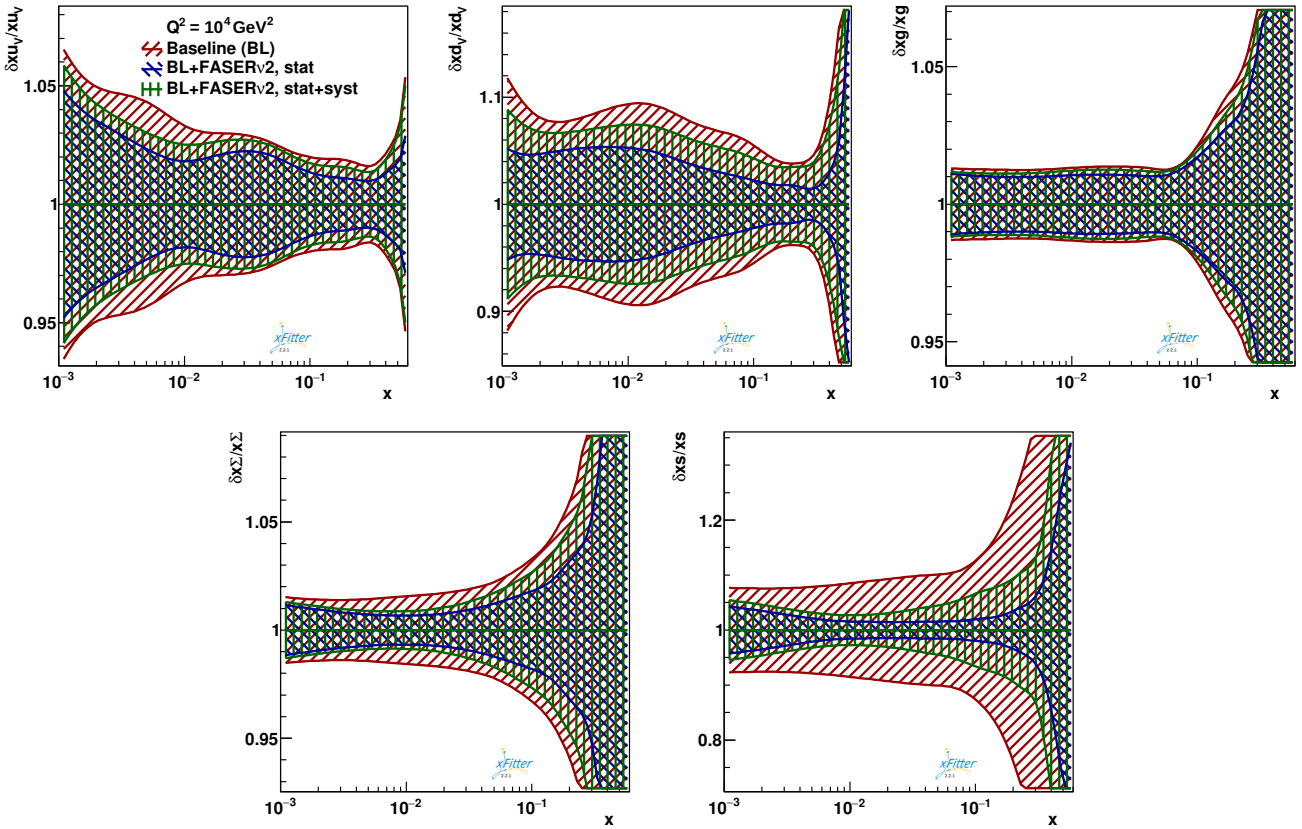


**Fig. 3.1.** The fractional PDF uncertainties (at the 68% confidence level) at  $Q^2 = 10^4 \text{ GeV}^2$  for the up and down valence quarks, gluon, total quark singlet, and total strangeness PDFs in the PDF4LHC21 baseline, compared to the results obtained once the FASER $\nu$ 2 structure functions are included. The FASER $\nu$ 2 impact projections are presented both without and with systematic uncertainties accounted for, and include charm-tagged structure functions as well as final-state lepton-charge separation.

for the up and down valence quarks, gluon, total quark singlet, and total strangeness PDFs in the PDF4LHC21 baseline, compared to the results obtained once the FASER $\nu$ 2 structure functions are added by means of Hessian profiling. The FASER $\nu$ 2 pseudo-data accounts for both inclusive and charm-tagged structure functions and assumes outgoing lepton- charge identification. We display results for the profiling in which the experimental covariance matrix considers only statistical uncertainties, as well as for the scenario where statistical and systematic errors are added in quadrature following the procedure spelled out in Sect. 2.4. We restrict the comparisons to the region  $10^{-3} \lesssim x \lesssim 0.7$  covered by the LHC neutrino experiments (see also Fig. 2.2). In addition of a reduction of PDF uncertainties, the Hessian profiling also results in general in a shift in the PDF central values. This shift is however arbitrary, since it depends on the fluctuations entering the pseudo-data generation, and is hence ignored in the following.

Inspection of Fig. 3.1 reveals that measurements of DIS structure functions at FASER $\nu$ 2 would reduce PDF uncertainties on the quark and antiquark PDFs, while leaving the gluon essentially unaffected. As expected for a neutrino scattering experiment, its impact is most marked

for those PDF combinations sensitive to quark flavour separation such as the up and down valence PDF as well as the total strangeness. Indeed, the reduction of PDF uncertainties is particularly significant for the latter, a consequence of the inclusion of charm-tagged structure functions in the fit. Given that all PDF determinations entering PDF4LHC21 already include existing neutrino DIS measurements, the fact that FASER $\nu$ 2 pseudo-data still manages to improve uncertainties highlights the new information provided by the LHC neutrino experiments.

By comparing the impact of the FASER $\nu$ 2 structure functions in the case where only statistical errors are considered with that where also systematic uncertainties are accounted for, one finds that the latter eventually become a limiting factor, but also that they not modify the qualitative findings of the statistics-only scenario. Indeed, while systematic uncertainties somewhat degrade the PDF sensitivity, they do not wash it out for any of the quark PDFs. Furthermore, in the projections presented in this work, we assume the performance parameters of Table 2.1, which however could be improved in the actual realisation of the experiments, using for instance detector improvements or different kinematic reconstruction techniques. We also note that the availability of complementary experiments access-

ing the same neutrino beam should allow their mutual cross-calibration, such that the combination of their data brings in more information than just the naive statistics scaling.

**Relevance of charm-tagged measurements.** The analysis of Fig. 3.1 highlights that LHC neutrino data is particularly constraining for the poorly-known strange PDF, which is one of the quark flavour combinations for which proton PDF fits differ the most [21]. To further investigate this point, Fig. 3.2 compares the impact of the FASER $\nu$ 2 data shown in Fig. 3.1, for the case in which only statistical uncertainties are considered, with the results of the same profiling once the charm-tagged structure function data is excluded from the fit. While differences are moderate for the up and down quark PDFs, the significant loss of information resulting from this exclusion of charm-tagged data is clearly visible for the strange PDF. Specially in the region  $x \gtrsim 0.01$ , the constraints on strangeness shown in Fig. 3.2 are mostly washed out in the absence of charm-tagged data. We thus establish that inclusive neutrino DIS measurements constrain predominantly the up and down quark and antiquark PDFs (and thus also the quark singlet), while the charm-tagged structure functions are responsible for most of the constraints provided on the total strangeness. The PDF reach of the LHC neutrino experiments would thus be markedly limited in experiments without charm-identification capabilities.

**Lepton-charge identification.** Being able to identify the charge of the produced final-state lepton in charged-current neutrino scattering demands equipping an experiment with a powerful enough magnet suitable to deflect this lepton within the detector fiducial volume. Our baseline results for FASER $\nu$ 2 in Fig. 3.1 assume that this charge-identification is possible, and therefore include separate structure function datasets for neutrino and anti-neutrino projectiles. In order to ascertain to which extent the constraints provided by FASER $\nu$ 2 structure functions depend on the availability of such a magnet, Fig. 3.3 compares the reduction of the PDF uncertainties using the FASER $\nu$ 2 data with and without assuming charged-lepton identification capabilities.

This analysis finds that the lack of charged-lepton identification actually does not degrade significantly the PDF sensitivity of FASER $\nu$ 2. Having access of the lepton charge information improves a bit the constraints for the down and (to a lesser extent) the up valence quark PDFs, while there are no differences for the total quark singlet and for strangeness. Such an improvement can be understood by inspecting the leading-order decomposition of neutrino DIS structure functions in terms of the different PDF flavours for different targets, Eqns. (2.5)–(2.7). For an isoscalar target, as assumed here, structure functions are very similar for neutrino and anti-neutrino projectiles, with differences restricted to the strangeness asymmetry. Given that this strangeness asymmetry is quite small, this also explains why the impact on strangeness, which is driven by the charm-tagged data, is the same irrespective of whether one

identifies the outgoing lepton charge. We conclude that LHC neutrino DIS data exhibits competitive PDF sensitivity even for detectors which cannot separate incoming neutrinos from antineutrinos.

**Experiment dependence.** Together with those for FASER $\nu$ 2, we have also produced PDF impact projections for other proposed FPF experiments, specifically for AdvSND and FLArE. In the latter case, we consider the 10 tonne variant FLArE10. Fig. 3.4 compares the PDF sensitivity of FASER $\nu$ 2, in the scenario where systematic uncertainties are neglected, with the corresponding results for AdvSND and FLArE10 respectively. As summarised by Table 2.2, each of these experiments has associated different expected numbers of DIS events, namely 510k, 56k, and 110k (670k) inclusive muon-neutrino events for FASER $\nu$ 2, AdvSND and FLArE10 (100) respectively, with 76k, 7k, and 15k (90k) in the charm-tagged case.

In agreement with expectations, detectors with the largest event rates are those exhibiting the best PDF sensitivity. From Fig. 3.4 one can see that the three FPF experiments studied lead to a reduction of the uncertainties in the quark PDFs. By comparing their relative impact, we find that the constraints achieved by FASER $\nu$ 2 are somewhat better than for the other two experiments, consistent with the larger event yields obtained in the former. In the case of AdvSND, the smaller sample of charm-tagged events is responsible for the reduction in the constraints on strangeness. Another consequence of the smaller event rates in AdvSND and FLArE10 as compared to FASER $\nu$ 2 is the milder impact for the  $x \lesssim 10^{-2}$  region, which can only be covered once the integrated statistics become large enough, as indicated by the differential bin-by-bin yields displayed in Fig. 2.1.

While Fig. 3.4 compares fits based on FPF pseudo-data with only statistical uncertainties, a more robust comparison between the PDF reach of the various FPF experiments requires accounting also for the systematic uncertainties, which ultimately become one of the limiting factors. Also, as mentioned above, cross-calibration between experiments should provide valuable input to enhance the PDF sensitivity.

Applying the same procedure to FASER $\nu$  and SND@LHC structure functions leaves the baseline results from PDF4LHC21 essentially unaffected, as demonstrated in App. A, and showing that for the current generation of LHC neutrino detectors it will be difficult to provide competitive constraints on the proton structure due to the (relatively) low DIS event rates.

**Combined impact of the FPF experiments.** We have also carried out a further PDF analysis including simultaneously the three FPF experiments considered here: FASER $\nu$ 2, AdvSND, and FLArE10. Fig. 3.5 displays the combined impact of the FPF experiments when added on top of the PDF4LHC21 baseline by means of Hessian profiling, both in the statistics-only case and when systematic and statistical uncertainties are added in quadrature. Potential

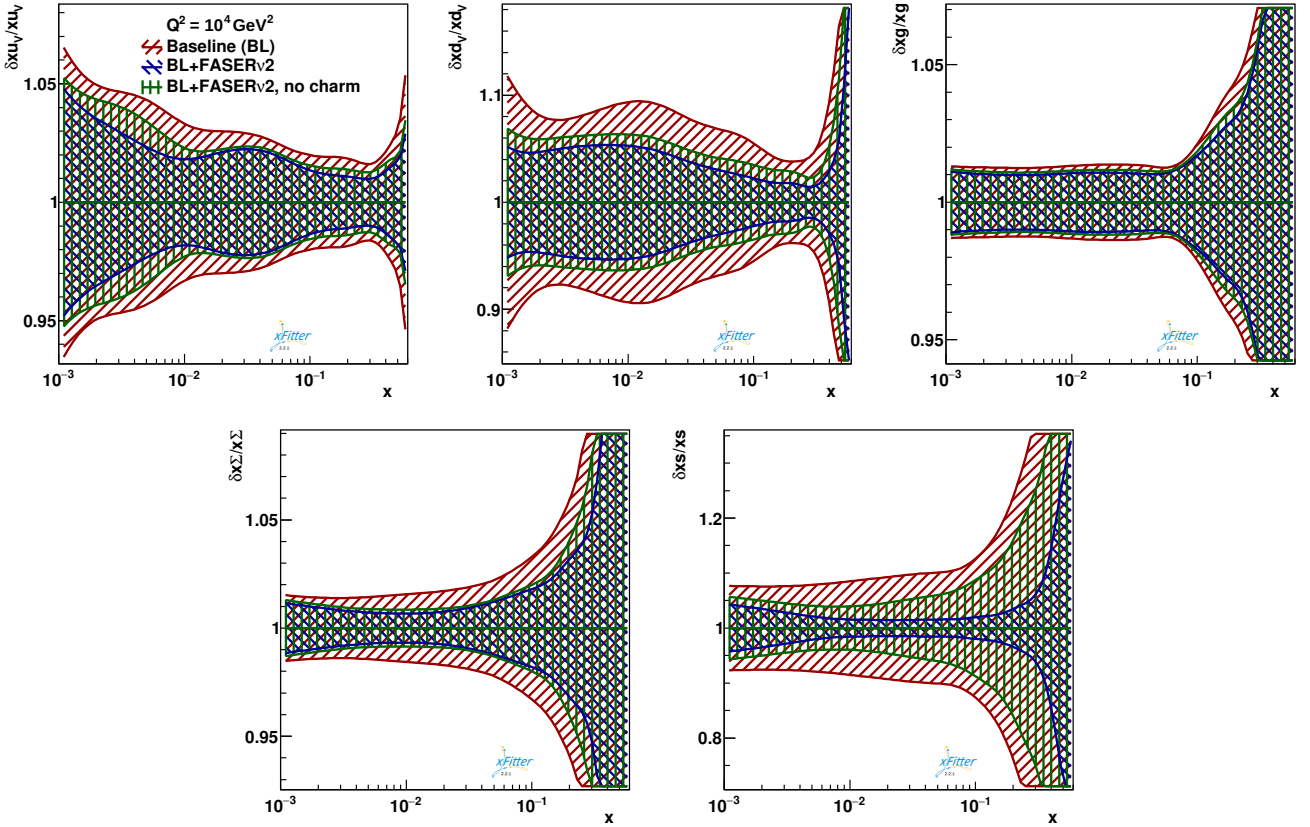


**Fig. 3.2.** Same as Fig. 3.1 (statistical uncertainties only), now showing results in the scenario where charm-tagged structure function measurements are excluded from the analysis.

correlations between individual experiments are neglected in this exercise. The combined impact of the three FPF experiments on PDF4LHC21 shown in Fig. 3.5 is only moderately improved as compared to the results of the FASER $\nu$ -only profiling in Fig. 3.1. This shows that in this combination of experiments the one with the largest individual sensitivity dominates, in this case FASER $\nu$ . Again, here we assume perfect consistency between theory and data, while within the actual experiments the consistency (or lack thereof) between individual measurements cannot be guaranteed.

The projections displayed in Fig. 3.5, and in particular the statistics-only case, represents a best-case scenario for the reduction of PDF uncertainties which can be expected from the analysis of neutrino DIS structure function data at the FPF, under the assumption that PDF4LHC21 represents our current knowledge about the quark and gluon structure of the proton.

### 3.2 Proton PDFs: impact on NNPDF4.0

The PDF sensitivity studies based on the xFITTER profiling of PDF4LHC21 are complemented by those based on their direct inclusion in the NNPDF4.0 analysis. Here we present results for the impact of the combined FPF neutrino measurements on NNPDF4.0, namely the analogous

study of that shown in Fig. 3.5 in the case of PDF4LHC21. We have also produced results for the different variations studied in Sect. 3.1 with the NNPDF fitting methodology. Given that the findings obtained with the NNPDF fits are compatible with those obtained with xFITTER, it is not necessary to duplicate them here and we only show results for the impact of the combined FPF pseudo-data.

Fig. 3.6 displays the same results as Fig. 3.5 now in the case of the fits obtained with the NNPDF4.0 fitting methodology. The baseline NNPDF4.0 NNLO analysis is compared with the results of the fits which include the combined FPF dataset, in both the statistics-only scenario and for the case where systematic uncertainties are also accounted for. As in the PDF4LHC21 analysis, the bands indicate the one-sigma PDF uncertainties. Note that we also show results for the charm PDF (bottom right panel), which in the NNPDF4.0 fit is also determined directly from the data entering the fit [88]. In this way, we can determine the possible constraints that neutrino DIS measurements at the LHC may impose on the intrinsic charm content of the proton [89].

From Fig. 3.6 one finds that the impact on the PDFs found by direct inclusion of the FPF structure functions on the NNPDF4.0 fit is qualitatively consistent with that found in the Hessian profiling of PDF4LHC21. In particular, the constraints are more significant for the up

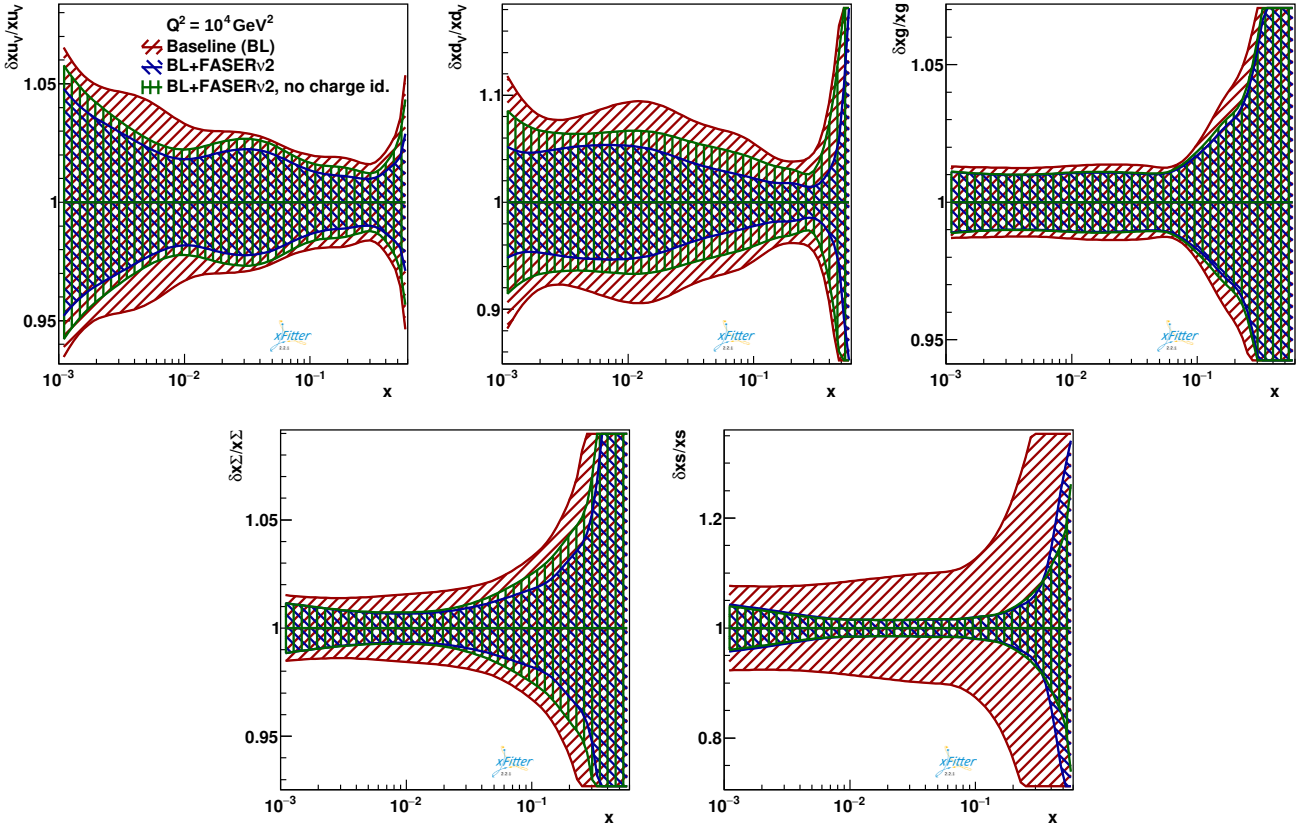


**Fig. 3.3.** Same as Fig. 3.1 (statistical uncertainties only), now showing results in the scenario where the charge of the final-state charged lepton cannot be identified.

and down quark valence PDFs as well as for the total strangeness. As was the case with PDF4LHC21, the uncertainty reduction for the strangeness is particularly striking. Also consistently with the results of Sect. 3.1, the gluon PDF is unchanged, and the impact on the total quark PDF is restricted to the large- $x$  region. While one can also identify differences related to analysis choices such as the PDF parametrisation and the method used to assess the PDF error reduction, for example, concerning the small- $x$  behaviour of  $xu_V$  and  $xd_V$ , we conclude that by and large the projected impact of the FPF structure function measurements is independent of the specific fitting methodology adopted.

As indicated by Fig. 3.6, the FPF data is also expected to reduce the uncertainties associated to the fitted charm PDF in the large- $x$  region dominated by the non-perturbative component. In order to highlight this impact on the large- $x$  region of the PDFs, Fig. 3.7 presents the same comparison as in Fig. 3.6 now for the absolute PDFs at the initial parametrisation scale,  $Q = 1.65$  GeV, using a linear scale, for the statistics-only scenario. One can observe the improved constraints on the charm PDF in the large- $x$  region, further confirming previous studies [9, 10] that indicate the sensitivity of the FPF to the intrinsic charm content of the proton. This comparison also illustrates the excellent constraining power on the proton

strangeness enabled by the FPF charm-tagged structure function data.

The statistical estimators for the NNPDF4.0 NNLO baseline fit, compared to the variants including the combined FPF dataset shown in Figs. 3.6 and 3.7, are reported in Table 3.1. The last row displays the  $\chi^2/n_{\text{dat}}$  obtained for the combined FPF dataset, for which one finds  $\chi^2/n_{\text{dat}} \sim 1$  up to fluctuations, consistent with the fact that the FPF pseudo-data is produced by construction to be compatible with the NNPDF4.0 baseline. For the same reason, the description of the other experiments entering the NNPDF4.0 global fit is not distorted by the inclusion of the FPF data. In particular, the  $\chi^2/n_{\text{dat}}$  of the available (non-FPF) DIS neutral-current and charged-current datasets is unchanged (1.22 and 0.90, respectively) from the baseline to the fit with FPF pseudo-data. A moderate increase is found to the  $\chi^2/n_{\text{dat}}$  of Drell-Yan processes, from 1.76 to 1.83, possibly because of the enhanced weight that DIS data carries in this fit variant.

Fig. 3.8 displays a comparison of the PDF luminosities at  $\sqrt{s} = 14$  TeV as a function of the final-state invariant mass  $m_X$  between the baseline NNPDF4.0 fit and its variants including the combined FPF dataset, see Fig. 3.6 for the corresponding PDF comparison. Results are shown normalised to the central value of the NNPDF4.0 baseline. Specifically, we show the gluon-gluon, quark-antiquark,

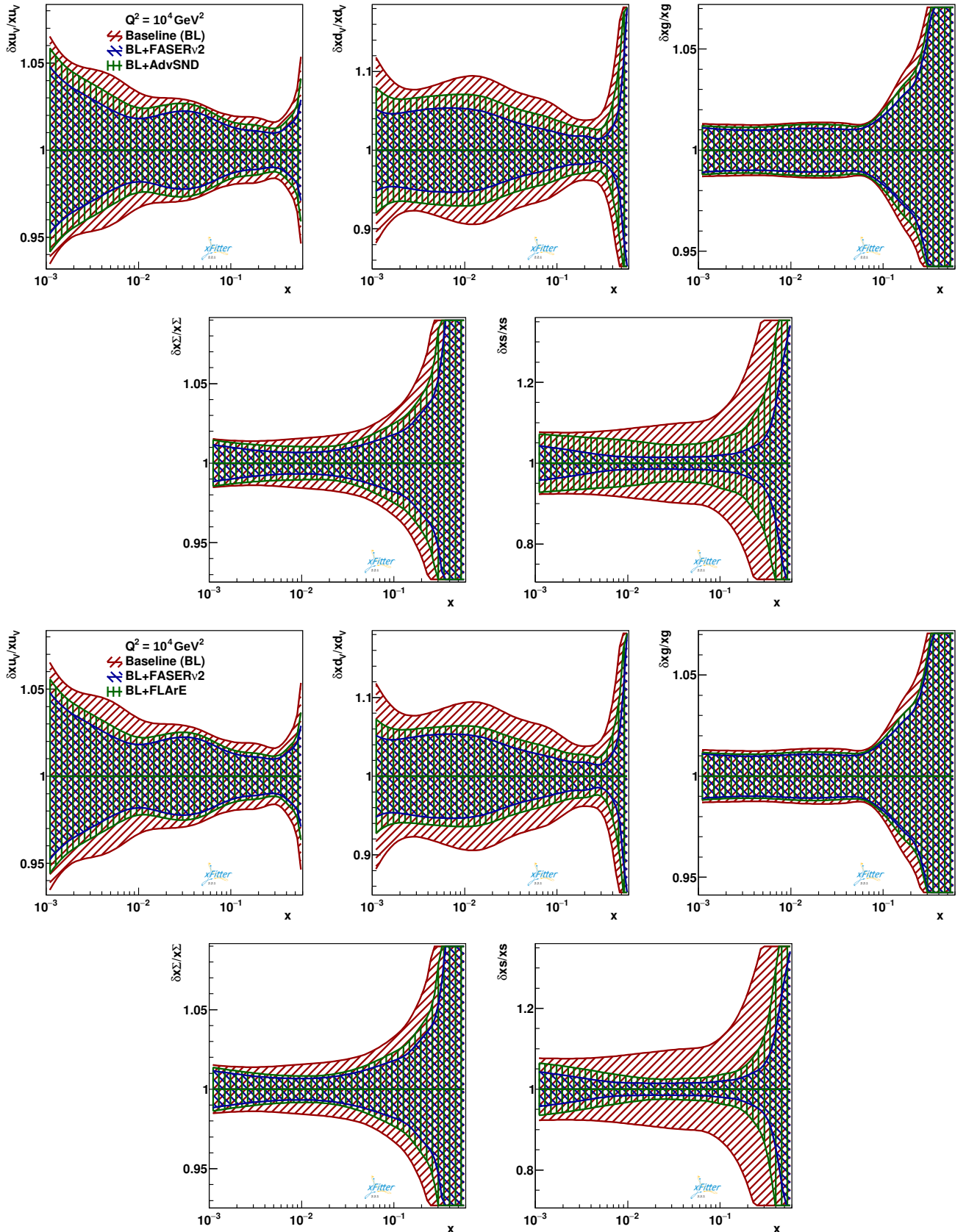


**Fig. 3.4.** Same as Fig. 3.1 (statistical uncertainties only), comparing the projected PDF impact of FASER $\nu$ 2 with that of AdvSND (top panels) and FLArE10 (bottom panels).

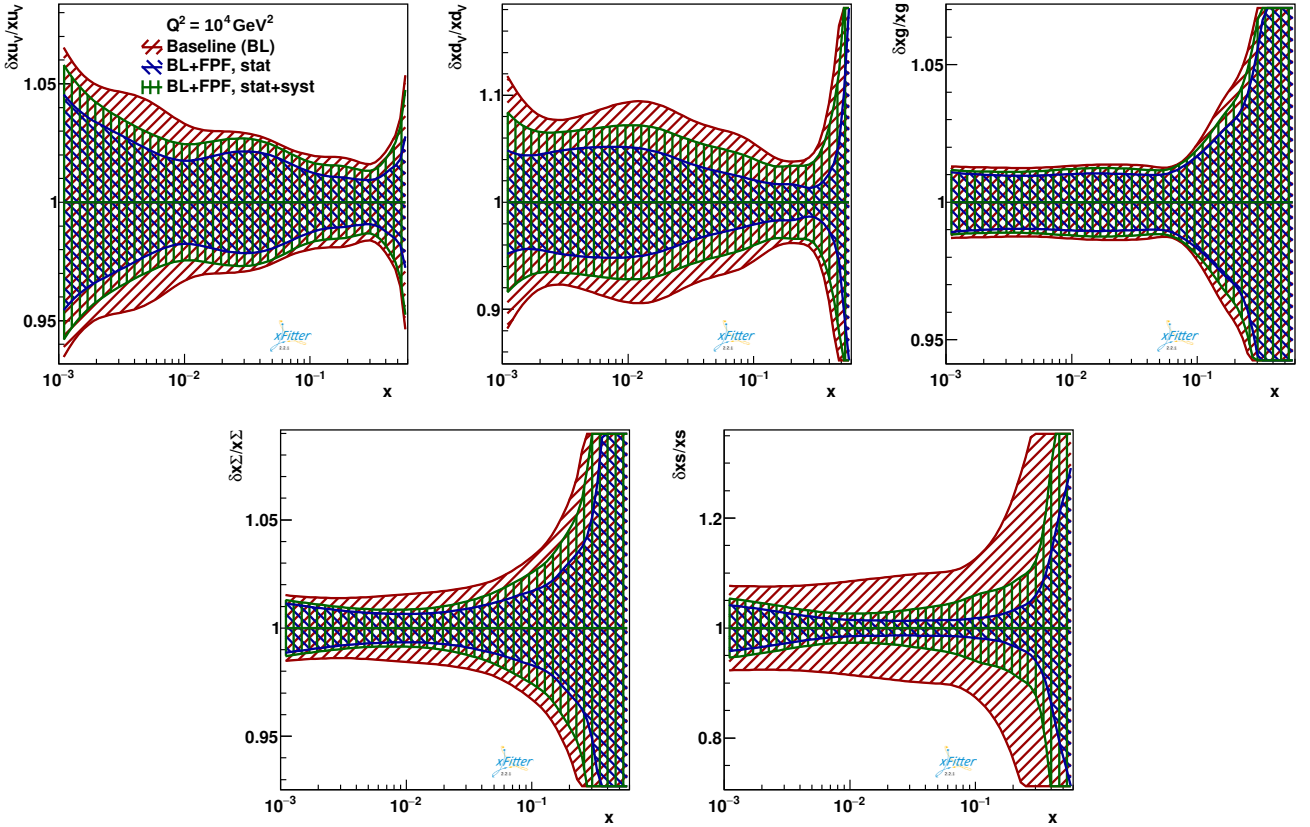


**Fig. 3.5.** Same as Fig. 3.1 now quantifying the projected PDF impact of the three FPF experiments added simultaneously to the analysis: FASER $\nu$ 2, AdvSND, and FLArE10.

quark-quark, down-antiup, up-antistrange, and strange-antistrange luminosities. The reduction of PDF uncertainties found in Figs. 3.6 and 3.7 is also visible for the partonic luminosities, specially in the best-case scenario where only statistical uncertainties in the FPF pseudo-data are considered. The improved quark-antiquark luminosities at  $Q \sim 100$  GeV benefit theoretical predictions for gauge-boson production at the LHC. It is also worth noting the PDF error reduction for the quark-quark luminosity at high invariant masses, which will feed into searches for new heavy particles at the TeV scale driven by quark-initiated scattering. Unsurprisingly, luminosities related to the strange PDF are those which improve the most, such as the  $u\bar{s}$  channel which provides a significant contribution to inclusive  $W^+$  production.

### 3.3 Nuclear PDFs: impact on EPPS21

The studies presented in Sects. 3.1 (for PDF4LHC21) and 3.2 (for NNPDF4.0) treat, from the point of view of PDF constraints, the neutrino scattering target as composed by isoscalar free-nucleons. They hence neglect both nuclear modifications and non-isoscalar effects. We now revisit these analyses but accounting for the fact that the target material in the FASER $\nu$ 2 and AdvSND experiments is tungsten, with  $A = 184$ . In this exercise we do not in-

clude the FLArE structure function data, corresponding to a different target material (liquid argon, with  $A = 40$ ), although in an actual nuclear PDF fit all FPF datasets would be included simultaneously. Nuclear modifications associated to a tungsten target, when compared to a free isoscalar nucleon, are not necessarily small, and will affect the event rate predictions for the FPF experiments. This fact also implies that measurements of differential neutrino cross-sections on heavy nuclear targets provide direct constraints on these nuclear modifications without relying on assumptions on their  $A$  dependence.

We quantify the impact of the FPF structure function measurements on the nuclear PDFs of tungsten by applying the same Hessian profiling of Sects. 3.1 to EPPS1, a global determination of nuclear PDFs that accounts for the constraints of existing datasets involving nuclei as target or projectiles, and based on the CT18 set as proton boundary condition. We note that EPPS21 already includes information from neutrino DIS on nuclear targets from the CHORUS and NuTeV experiments. EPPS21 is generally in good agreement with other recent nPDF fits such as nNNPDF3.0 [32] and nCTEQ15HQ [90].

The application of profiling to EPPS21 follows the same strategy as that for PDF4LHC21, with the caveat that its Hessian error sets also include the contribution from the uncertainties associated to their reference proton PDF

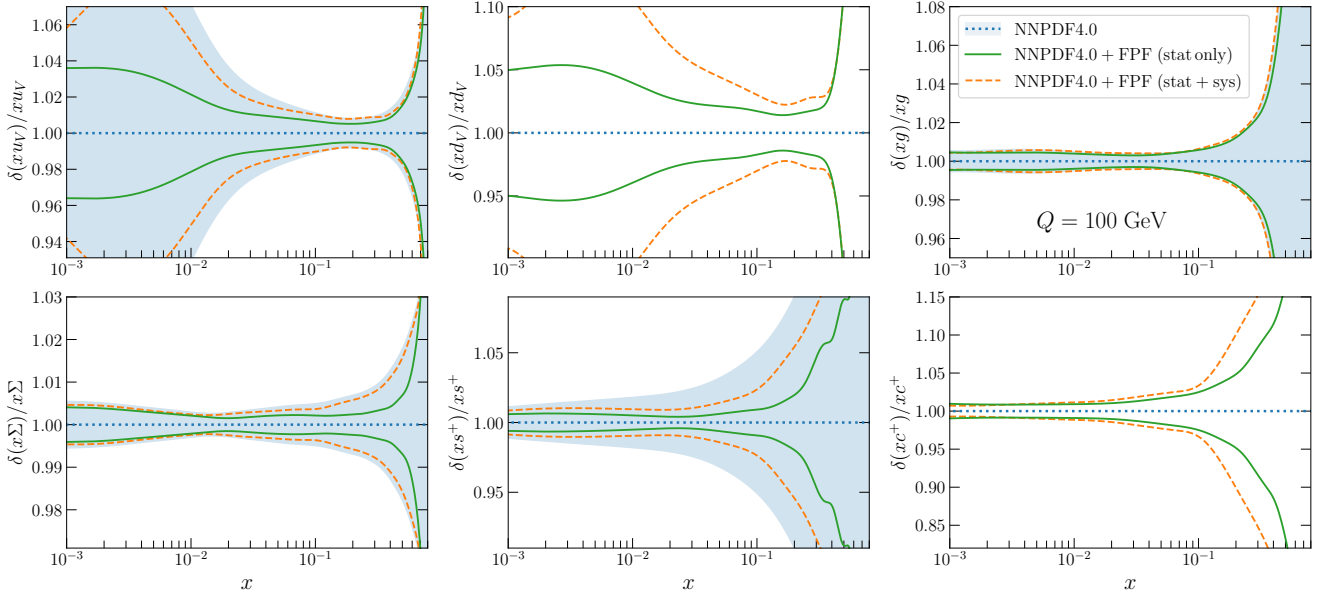


**Fig. 3.6.** Same as Fig. 3.5 for the results obtained using the NNPDF4.0 fitting methodology. The baseline NNPDF4.0 NNLO analysis is compared with the results of the fits which include the combined FPF dataset in both the statistics-only scenario and for the case where systematic uncertainties are also accounted for. As in the PDF4LHC21 case, we now also show results for the charm PDF (bottom right panel), which in the NNPDF4.0 fit is determined from the data entering the fit.

	Dataset	NNPDF4.0 NNLO		
		Baseline	with combined FPF data	
			Statistical-only	Statistical + systematics
$\chi^2/n_{\text{dat}}$		1.17	1.15	1.14
$\langle E_{\text{tr}} \rangle_{\text{rep}}$	Global	2.26	2.24	2.21
$\langle E_{\text{val}} \rangle_{\text{rep}}$		2.36	2.33	2.30
$\langle \chi^2/n_{\text{dat}} \rangle_{\text{rep}}$		1.19	1.18	1.16
$\chi^2/n_{\text{dat}}$	DIS neutral-current	1.22	1.23	1.22
	DIS charged-current	0.90	0.91	0.90
	Drell-Yan (inclusive and one-jet)	1.76	1.84	1.83
	Top-quark pair production	1.23	1.19	1.25
	Single-top production	0.36	0.37	0.37
	Inclusive jet production	0.96	0.96	0.94
	Dijet production	2.03	2.03	2.00
	Direct photon production	0.74	0.74	0.73
	FPF (total)	1.29 / 0.92	1.10	0.89

**Table 3.1.** Statistical estimators for the NNPDF4.0 NNLO baseline fit, compared to the variants including the combined FPF dataset shown in Figs. 3.6 and 3.7. From top to bottom: total  $\chi^2/n_{\text{dat}}$ , average over replicas of the training and validation figures of merit  $\langle E_{\text{tr}} \rangle_{\text{rep}}$  and  $\langle E_{\text{val}} \rangle_{\text{rep}}$ , average  $\chi^2/n_{\text{dat}}$  over replicas  $\langle \chi^2/n_{\text{dat}} \rangle_{\text{rep}}$ ,  $\chi^2/n_{\text{dat}}$  for datasets grouped by process. The last row displays the  $\chi^2/n_{\text{dat}}$  obtained for the combined FPF dataset. For the baseline, we indicate the pre-fit values of  $\chi^2/n_{\text{dat}}$  for the FPF dataset (in italics) computed without and with systematic errors in the covariance matrix.

set, in this case CT18. Given that the measured event rates depend on both the proton PDFs and the nuclear

modifications, when profiling EPPS21 we also account for the Hessian sets associated to the proton PDF dependence.

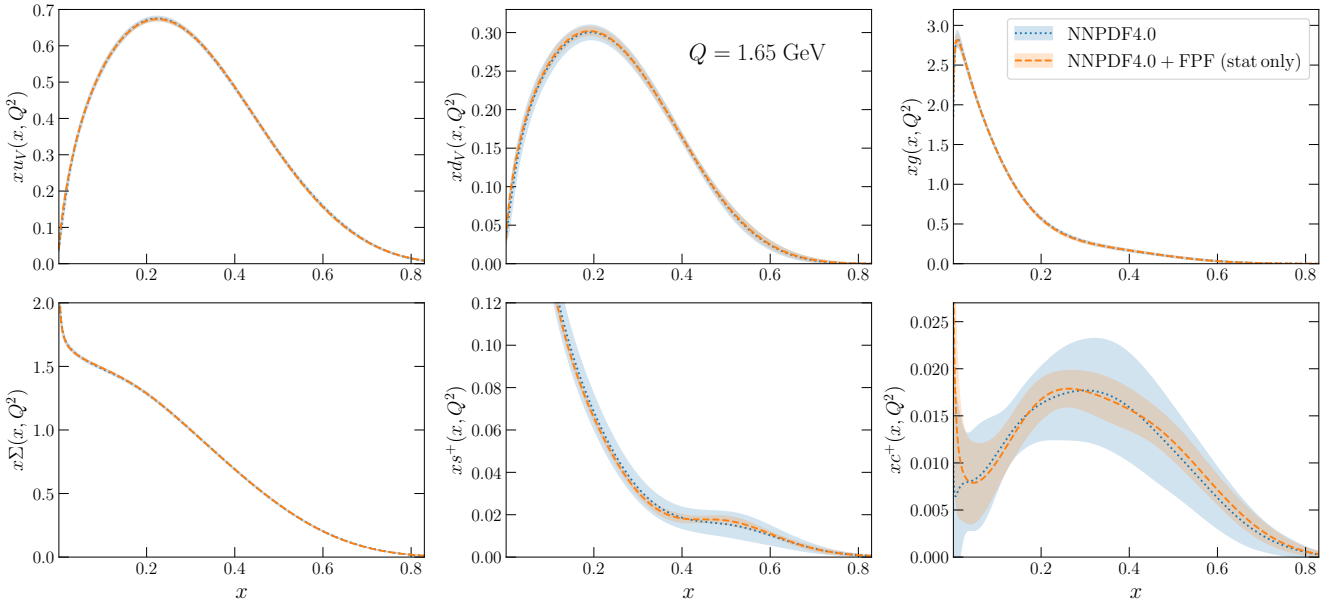


**Fig. 3.7.** Same as Fig. 3.6 now for the absolute PDFs at the initial parametrisation scale,  $Q = 1.65$  GeV, focusing on the large- $x$  region.

Also relevant for the subsequent discussion, EPPS21 adopts a tolerance factor of  $T^2 = 20$  when defining their 68% confidence level uncertainties, to be contrasted with  $T^2 = 10$  used in PDF4LHC21.

Fig. 3.9 displays a similar comparison as that of Fig. 3.5, now corresponding to the Hessian profiling of EPPS21 for a tungsten nucleus. The FPF dataset is in this case composed by FASER $\nu$ 2 and AdvSND. One finds that the impact of FPF structure function measurements is most important for the strange PDF, and to a lesser extent for the up and down valence quark PDFs. For the latter, the projected impact of FPF measurements appears to be somewhat milder as in the case of PDF4LHC21, especially once systematic uncertainties are taken into account.

While the main qualitative features of the nPDF profiling are consistent with the free-proton case, one reason explaining the observed differences may be the usage of a larger tolerance factor  $T$  in EPPS21 as compared to PDF4LHC21, which effectively reduces the impact of new data in the fit. Another potential reason is the more restrictive functional form adopted in EPPS21 as compared to the PDF sets entering PDF4LHC21, a consequence of the smaller dataset available for hard scattering on nuclear targets. Given that these functional forms are fixed when applying Hessian profiling, assessing the impact on a nuclear PDFs by a direct refit, as was done for NNPDF4.0, may be required to establish the impact of FPF structure function data on nPDFs. Additional results for the profiling of EPPS21 are presented in App. B.

## 4 Implications for Higgs and weak boson production

The reduction of PDF uncertainties made possible by neutrino DIS measurements at the FPF, discussed in Sect. 3, enables more precise theoretical predictions for core processes at the HL-LHC. Here we present an initial study of the phenomenological implications of the PDFs enhanced with LHC neutrino data for hard-scattering processes at proton colliders. Specifically, we present results for single and double gauge boson production, Higgs production in vector-boson fusion, and Higgs production and in association with a vector boson. We focus on processes sensitive to the quark-quark and quark-antiquark initial states, given that LHC neutrinos do not provide information on the gluon PDF and hence they cannot inform gluon-initiated processes, such as top quark pair production or Higgs production in gluon fusion.

We adopt the same calculational settings as in the LHC phenomenology analysis considered in the PDF4LHC21 combination study [46] and provide predictions both for inclusive cross-sections, integrated in the fiducial region, and for differential distributions. We evaluate these cross-sections using matrix elements which include NLO corrections both in the QCD and electroweak coupling using MG5\_AMC@NLO [91] interfaced to PINEAPPL [55]. For all processes, realistic selection and acceptance cuts on the final state particles have been applied. No further theory uncertainties are considered in this analysis, given that we don't aim to compare with experimental data.

Fig. 4.1 displays fiducial cross-section for representative LHC processes at  $\sqrt{s} = 14$  TeV evaluated with NNPDF4.0 (top panels) and with PDF4LHC21 (bottom panels), compared with the results obtained from the corresponding

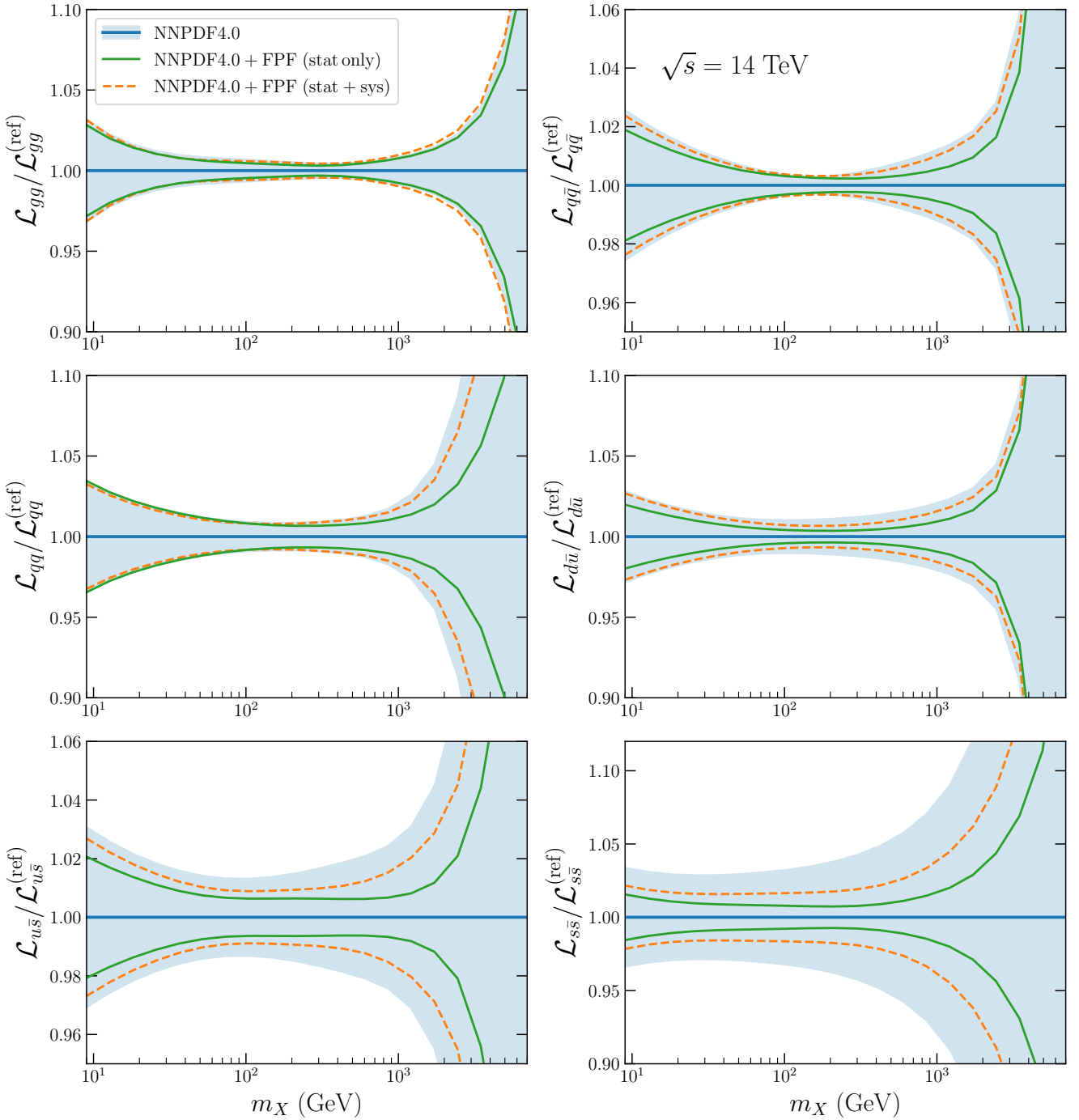


**Fig. 3.8.** Comparison of the PDF luminosities evaluated at  $\sqrt{s} = 14 \text{ TeV}$  as a function of the final-state invariant mass  $m_X$  between the baseline NNPDF4.0 NNLO determination and its variants which include the full set of FPF pseudo-data, see Figs. 3.6 for the corresponding PDF comparison. Results are shown normalised to the central value of the NNPDF4.0 baseline. From left to right and top to bottom we show the gluon-gluon, quark-antiquark, quark-quark, down-antiuip, up-antistrange, and strange-antistrange luminosities. The bands in the NNPDF4.0 baseline indicate the one-sigma PDF uncertainties.

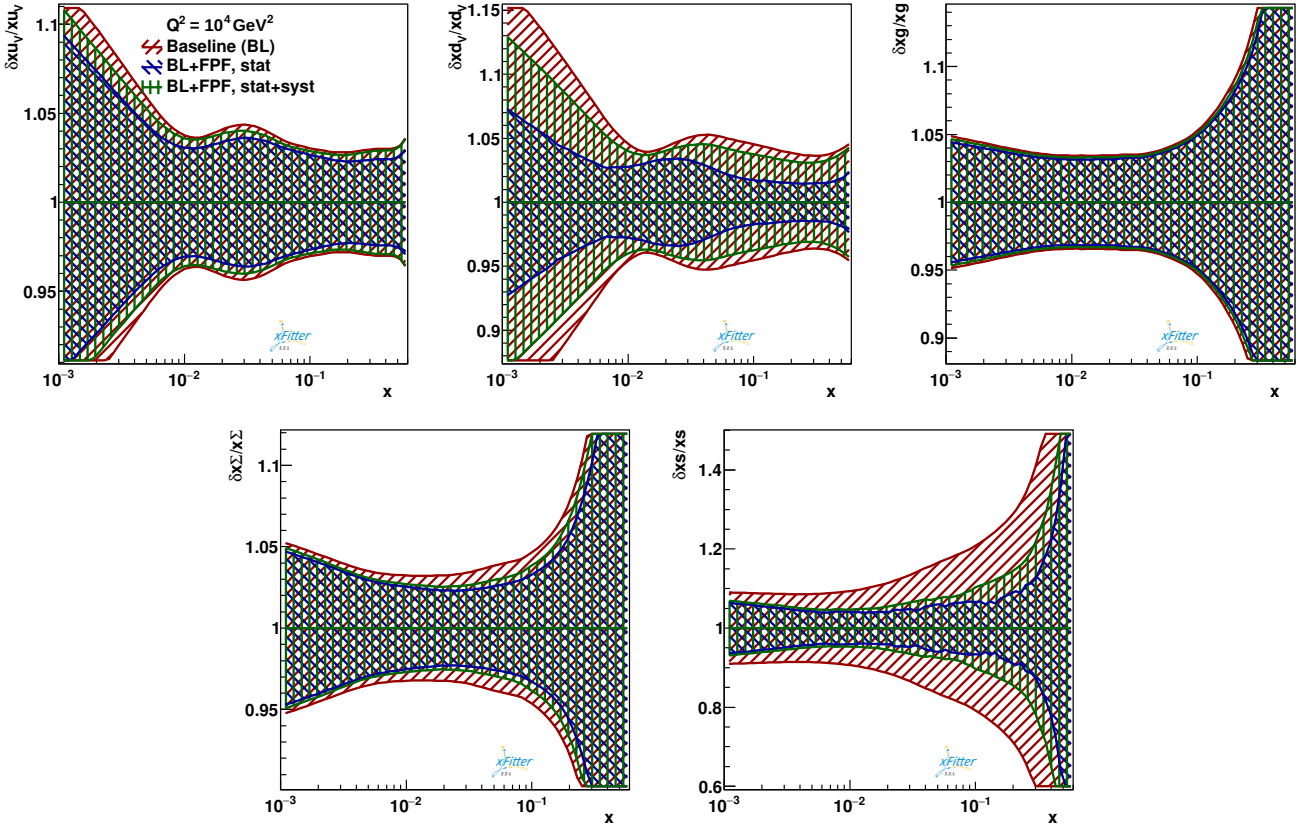


**Fig. 3.9.** Same as Fig. 3.5 now corresponding to the Hessian profiling of EPPS21 for a tungsten nucleus, and excluding FLArE contributions.

fits including the FPF structure function projections. For the fits with FPF data we display the variants where the covariance matrix consists only of statistical errors (“\_FPF\*”) and where also systematic errors are accounted for (“\_FPF”). For the baseline predictions, the dark (light) bands indicate the 68% (95%) CL uncertainties. The central values are set to be the same as in the baseline calculation in all cases. From top to bottom, we show inclusive Drell-Yan production in the  $Z$ ,  $W^+$ , and  $W^-$  channels, Higgs production in vector-boson fusion, Higgs associated production, and diboson production in the  $W^+W^-$ ,  $W^+Z$ , and  $W^-Z$  final-states. The corresponding comparisons at the level of differential distributions are shown in Figs. 4.2 and 4.3 for NNPDF4.0 and PDF4LHC21 respectively. As done for the fiducial cross-sections of Fig. 4.1, we only indicate the relative PDF uncertainty in each fit.

Inspection of Figs. 4.1–4.3 confirms the potential of LHC neutrino structure function measurements to improve theoretical predictions for Higgs, electroweak and high-mass processes at the HL-LHC. In general, qualitative consistency between the results based on NNPDF4.0 and on PDF4LHC21 is found, as was already the case at the PDF level. As compared to the best-case scenario where only statistical uncertainties are taken into account, the reduction of PDF errors in the LHC cross-sections obtained thanks for the FPF structure functions becomes

less marked, but still visible for most of the processes under consideration, upon the inclusion of systematic uncertainties in the fit covariance matrix.

Concerning the fiducial integrated cross-sections, a decrease in PDF uncertainties is observed for all processes, including for single gauge boson production relevant for core HL-LHC analyses such as the  $m_W$  and  $\sin^2 \theta_W$  measurements. The specific improvement in precision depends on the underlying scattering reaction as well as on the range of  $x$  and  $Q^2$  covered by each process. In the case of Higgs associated production with vector bosons and in vector-boson scattering, driven by the quark-antiquark and quark-quark initial states respectively, one observes that PDF uncertainties can be reduced by up to a factor two thanks to the FPF measurements, for instance in the case of the  $hW^+$  and  $hW^-$  cross-sections, in the most optimistic scenario in which systematic uncertainties are neglected. Likewise for the diboson cross-sections, with in this case the largest improvement observed for the  $ZW^+$  and  $ZW^-$  final states, with a reduction of up to  $\sim 40\%$  in the PDF uncertainties.

In the case of the differential cross-sections displayed in Figs. 4.2 and 4.3, one observes how the impact of the FPF structure functions on LHC observables depends on the hard-scattering scale. For instance, searches for heavy resonances in the high-mass tail of the Drell-Yan distribu-

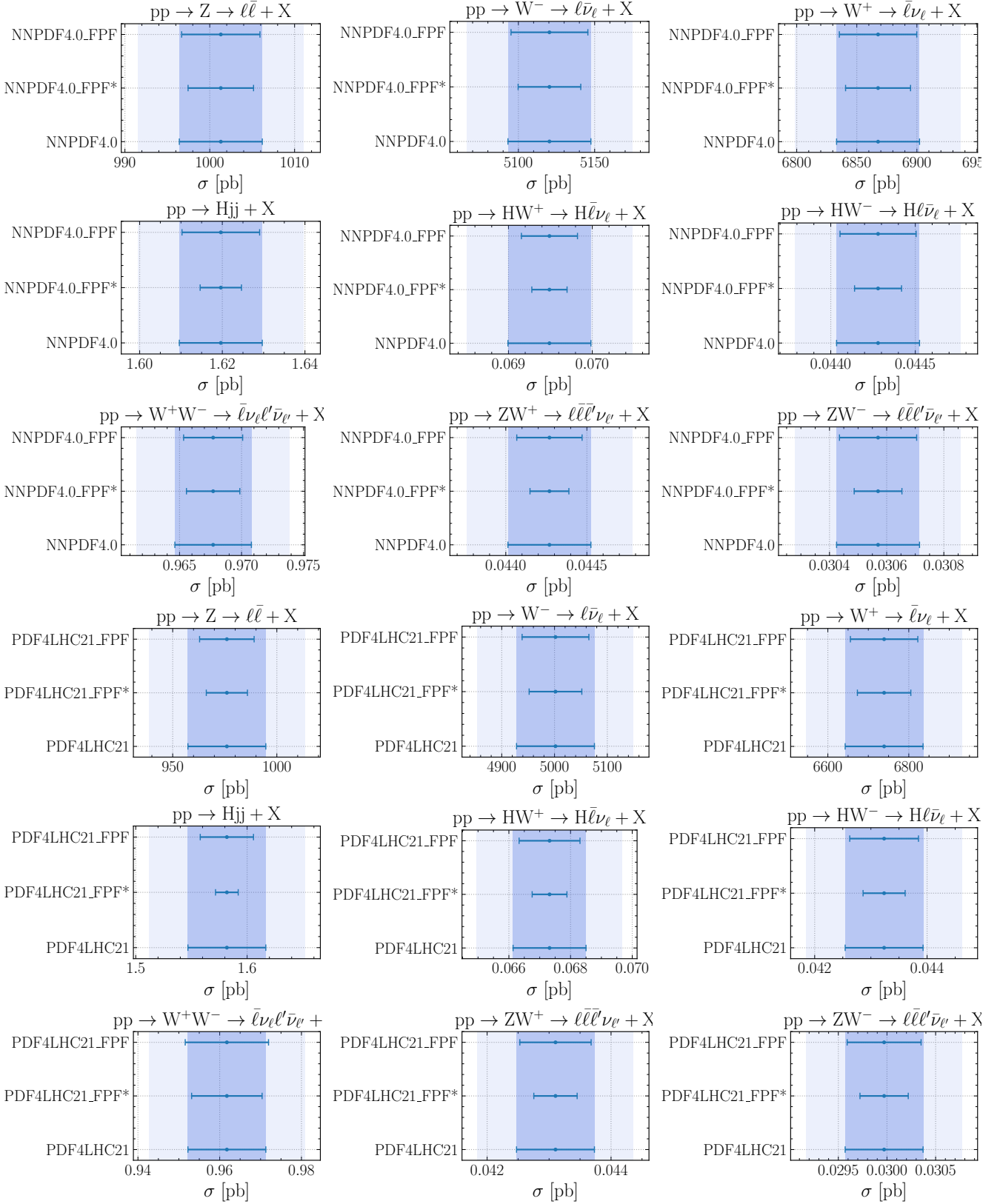


**Fig. 4.1.** Fiducial cross-sections for representative LHC processes at  $\sqrt{s} = 14$  TeV evaluated with NNPDF4.0 (upper panels) and PDF4LHC21 (bottom panels), compared with the fits including the FPF structure function projections. See [28, 46] for the calculational settings used to evaluate these cross-sections. For the baseline predictions, the dark (light) bands indicate the 68% (95%) CL uncertainties. The fits labelled as “\_FPF\*” are the ones considering statistical uncertainties, while those labelled as “\_FPF” also include systematic errors. In the fits with FPF data, the central values are set to be the same as in the corresponding baseline. We provide predictions for inclusive Drell-Yan production ( $Z, W^+, W^-$ ), Higgs production in vector-boson fusion, Higgs associated production ( $W^+W^-$ ,  $W^+Z$ ,  $W^-Z$ ).

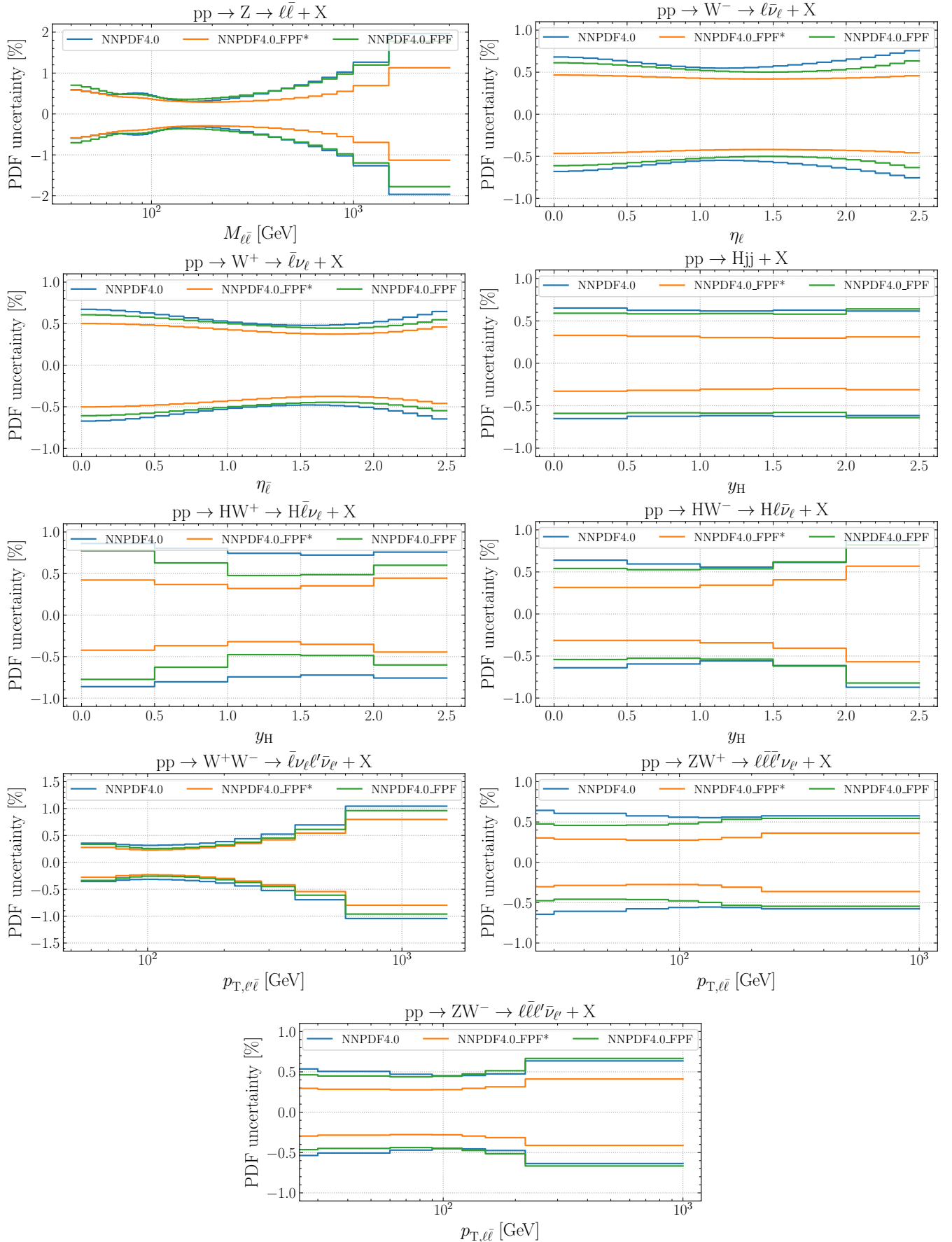


**Fig. 4.2.** Same as Fig. 4.1 for the corresponding differential distributions in the case of NNPDF4.0

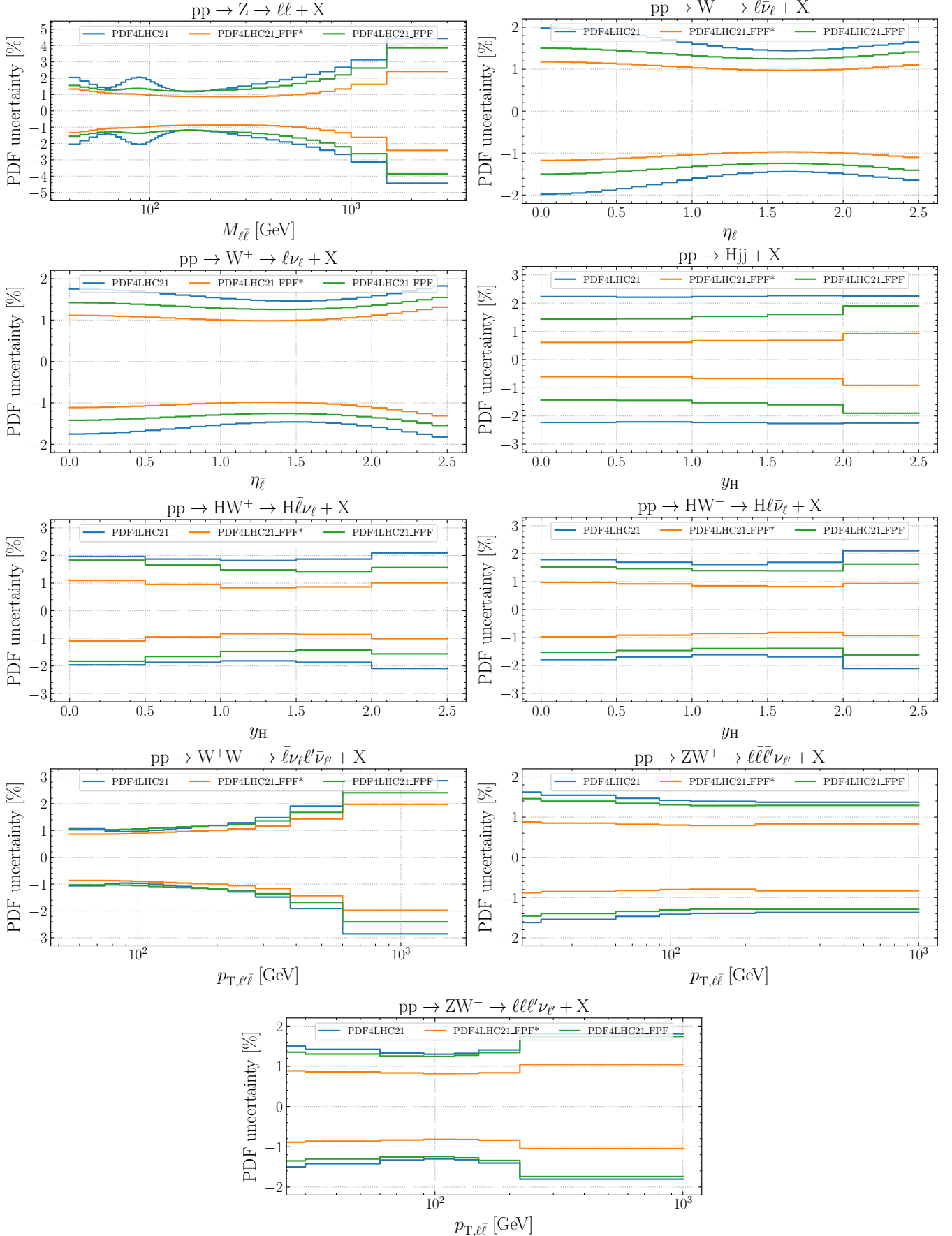


**Fig. 4.3.** Same as Fig. 4.2 but with PDF4LHC21.

tions could be improved by the addition of the FPF data. Similar considerations apply for diboson prediction, and in the case of the  $ZW^\pm$  channel we observe an improvement specially in the low  $p_{T,\ell\ell}$  region which represents the bulk of the fiducial cross-sections. For the Higgs production processes, the PDF uncertainty in the theory predictions is relatively stable as a function of the rapidity. The effects of accounting for systematic uncertainties in the fit covariance matrix are somewhat more visible here as compared to the inclusive cross-sections, indicating that they affect mostly the tails, rather than the bulk, of the distributions, and in particular the large- $x$  behaviour of the PDFs. This observation emphasizes the importance of reducing systematic errors in the FPF measurements in order to enhance the cross-talk with HL-LHC analyses.

## 5 Summary and outlook

In this work we have, for the first time, quantified the impact that measurements of high-energy neutrino DIS structure functions at the LHC would have on the quark and gluon structure of the nucleon. Our analysis requires the generation of DIS pseudo-data fully differential in  $x$ ,  $Q^2$ , and  $E_\nu$  for the various ongoing and proposed far-forward neutrino LHC experiments, including the estimate of their associated systematic uncertainties. Consistent results are obtained from both the Hessian profiling of PDF4LHC21 and from the direct inclusion of LHC neutrino structure functions in the NNPDF4.0 global fit, revealing a reduction of PDF uncertainties in the light quark sector, in particular concerning strangeness, as well as for the large- $x$  charm PDF in the case of NNPDF4.0. We have assessed the robustness of these results upon removing charm-tagged data and final-state lepton-charge identification, as well as upon the combination of all FPF experiments within a single analysis.

We have also demonstrated the rich interplay between far-forward and central measurements at the HL-LHC by providing predictions for a range of Higgs and gauge boson production processes, both for integrated cross-sections in the fiducial region and for single-differential distributions. This phenomenological analysis suggests that a reduction of the PDF uncertainty by up to a factor two may be within reach for some of these cross-sections in the most optimistic scenario. As was the case at the PDF level, also for the HL-LHC projections results based on PDF4LHC21 and NNPDF4.0 are in qualitative agreement.

Several avenues extending the results of this work may be foreseen. First of all, as the design of the proposed FPF experiments advances, it will be possible to derive more accurate estimates of the systematic uncertainties (and of their correlations) which eventually become the limiting factor. This will allow studying whether improved detection methods, novel reconstruction techniques i.e. based on deep learning, or combining information from different experiments can push down the systematic uncertainties affecting the measurements. Second, the modelling of neutrino scattering at the LHC would benefit from the use

of Monte Carlo event generators accounting for higher-order QCD corrections. As compared to the currently used LO generators, these would improve the description of the final-state kinematics, which in turn determine the acceptance rate of the reconstructed events. Furthermore, the predictions from such precise Monte Carlo generators should be folded with a full-fledged detector simulation in order to robustly determine selection efficiencies, e.g. such as those related to charm and  $D$ -meson tagging.

Third, while here we focus on the DIS region, ongoing and future LHC neutrino experiments also provide important information on shallow-inelastic scattering (SIS) at lower values of  $Q$  [15, 92], which in turn are relevant for inclusive cross-sections entering atmospheric and oscillation neutrino experiments. By following the approach presented in this work, it should be possible to quantify the improvements that LHC data provides on models of neutrino scattering in this poorly-understood SIS region. Finally, here we have taken the incoming neutrino fluxes as an external input and neglected any associated uncertainties. However, measurements of these fluxes provide unique information on light and heavy forward hadron production in QCD, and in particular open a new window to the small- $x$  gluon PDF. For this reason, ultimately one needs to simultaneously constrain the incoming fluxes and the neutrino scattering cross-sections from the measured event rates. Such joint interpretation would require extending the present analysis with a data-driven parametrisation of the neutrino fluxes, which could subsequently be compared with different theoretical predictions.

Our findings highlight how exploiting the LHC neutrino beam for hadron structure studies effectively provides CERN with a “Neutrino-Ion Collider”, a charged current-counterpart of the EIC, without changes in its accelerator infrastructure or additional energy costs. In addition for their intrinsic interest for hadronic science, measurements of neutrino structure function at the LHC provide a novel, and until now ignored, handle to inform theoretical predictions of hard-scattering cross-sections at the HL-LHC.

---

Together with this paper, we make public in Zenodo [93] the corresponding LHAPDF grids [94] for the PDF4LHC21 and NNPDF4.0 fits including FPF data. We also release the generated neutrino structure function pseudo-data and the corresponding theory calculations, for the different scenarios considered in this work. These projections for neutrino structure functions should be of relevance for a broad range of applications related to forward neutrino scattering at the LHC, from tests of lepton flavour universality at the TeV scale in the neutrino sector to probes of anomalous neutrino interactions and searches for sterile neutrinos distorting oscillation patterns.

## Acknowledgments

We are grateful to many colleagues involved in the Forward Physics Facility initiative for illuminating discussions and

encouragement along the course of this project, in particular Jamie Boyd, Jonathan Feng, and Albert de Roeck. We thank specially Felix Kling for many useful discussions and for providing updated predictions for the neutrino fluxes. We thank Akitaka Ariga and Tomoko Ariga for discussion concerning FASER $\nu$ 2, Milind Diwan, Wenjie Wu, and Steven Linden concerning FLArE, and Antonia di Crescenzo for information concerning AdvSND. We thank Christopher Schwan, Simone Amoroso and Xiaomin Shen for useful discussions regarding the implementation and testing of the PINEAPPL interface to xFITTER. We also thank Emanuele R. Nocera for providing us with the EIC pseudodata.

The work of M. F. was supported by NSF Grant PHY-2210283 and was also supported by NSF Graduate Research Fellowship Award No. DGE-1839285. The work of T. G., G. M., and J. R. is partially supported by NWO, the Dutch Research Council. The work of T. R. and J. R. is partially supported by an ASDI2020 Fellowship from the Netherlands eScience Center. The work of T. M is supported by the National Science Centre, Poland, research grant No. 2021/42/E/ST2/00031.

## A Impact of FASER $\nu$ Run III measurements

The same procedure applied to the FPF experiments in Sect. 3.1 can also be used in the case of FASER $\nu$ , for which pseudo-data is generated for a Run III integrated luminosity of  $\mathcal{L} = 150 \text{ fb}^{-1}$ . As indicated by Table 2.2, by the end of Run III, one expects that FASER $\nu$  will have recorded around 600 and 1800 electron- and muon-neutrinos respectively corresponding to deep-inelastic scattering events, of which around 100 and 300 respectively are associated to charm-tagged events. These projected event rates can be compared with the expectations for FASER $\nu$ 2, which predict an increase in statistics of more than two orders of magnitude.

Fig. A.1 presents a similar comparison as that of Fig. 3.1 now between the projected PDF impact of FASER $\nu$ 2 and that of FASER $\nu$ . One finds that neutrino DIS measurements at FASER $\nu$  are unable to improve PDF uncertainties as compared to the baseline scenario encapsulated by PDF4LHC21. The reason is two-fold: the smaller event rates as compared to FASER $\nu$ 2, and the reduced coverage of the  $(x, Q^2)$  phase space shown in Fig. 2.1. The differences in PDF sensitivity between FASER $\nu$  and FASER $\nu$ 2 in Fig. A.1 illustrate the importance of realising the FPF in order to exploit the full physics potential enabled by LHC neutrinos for QCD and hadron structure studies.

It should be emphasized that the lack of PDF sensitivity displayed in Fig. A.1 does not imply that measuring DIS structure functions at FASER $\nu$  will not provide useful information. First of all, our procedure assumes perfect compatibility between current data and the projected DIS neutrino measurements at the LHC, something which remains to be demonstrated experimentally. Second, FASER $\nu$  still covers a region of neutrino energies unexplored by previous experiments, hence providing a new validation of our QCD calculations and of neutrino

interactions at the TeV scale. Third, it would represent a non-trivial proof-of-concept that LHC neutrino differential measurements can be unfolded to the cross-section level to be used in theoretical interpretations, paving the way and demonstrating the feasibility of subsequent neutrino DIS measurements at the FPF experiments.

## B Additional nPDF impact studies

The impact of FPF structure function measurements on the EPPS21 nuclear PDF determination has been studied in Sect. 3.3. Here we provide additional results from this study, and specifically quantify the impact that removing charm-tagged structure functions and flavour-charge identification capabilities would have on the projected results. Fig. B.1 displays the analogous comparisons as in Figs. 3.2 and 3.3 in the case of EPPS21. In both cases, results are consistent with the proton PDF profiling analysis.

First of all, charm-tagged events are essential to achieve the best sensitivity to the strange PDF, while they have a vanishing impact on the other PDF combinations. Second, not being able to identify the charge of the outgoing final-state lepton does not markedly affect the baseline results, with the possible exception of the down valence quark PDF. As discussed in Sect. 2.1, for a non-isoscalar target such as tungsten, with  $Z = 74$  and  $A - Z = 110$ , event rates with neutrino projectiles will differ from those arising from antineutrino scattering, introducing additional information as compared to an isoscalar target in terms of PDF sensitivity.

## References

1. F. Kling and L. J. Nevay, “Forward neutrino fluxes at the LHC,” *Phys. Rev. D* **104** no. 11, (2021) 113008, [arXiv:2105.08270 \[hep-ph\]](https://arxiv.org/abs/2105.08270).
2. **FASER** Collaboration, H. Abreu et al., “First Direct Observation of Collider Neutrinos with FASER at the LHC,” *Phys. Rev. Lett.* **131** no. 3, (2023) 031801, [arXiv:2303.14185 \[hep-ex\]](https://arxiv.org/abs/2303.14185).
3. **SND@LHC** Collaboration, R. Albanese et al., “Observation of Collider Muon Neutrinos with the SND@LHC Experiment,” *Phys. Rev. Lett.* **131** no. 3, (2023) 031802, [arXiv:2305.09383 \[hep-ex\]](https://arxiv.org/abs/2305.09383).
4. **FASERcollaboration** Collaboration, “Observation of high-energy electron neutrino interactions with FASER’s emulsion detector at the LHC,” tech. rep., CERN, Geneva, 2023. <https://cds.cern.ch/record/2868284>.
5. **FASER** Collaboration, H. Abreu et al., “Detecting and Studying High-Energy Collider Neutrinos with FASER at the LHC,” *Eur. Phys. J. C* **80** no. 1, (2020) 61, [arXiv:1908.02310 \[hep-ex\]](https://arxiv.org/abs/1908.02310).
6. **FASER** Collaboration, H. Abreu et al., “The FASER Detector,” [arXiv:2207.11427 \[physics.ins-det\]](https://arxiv.org/abs/2207.11427).
7. **SHiP** Collaboration, C. Ahdida et al., “SND@LHC,” [arXiv:2002.08722 \[physics.ins-det\]](https://arxiv.org/abs/2002.08722).
8. **SND@LHC** Collaboration, G. Acampora et al., “SND@LHC: The Scattering and Neutrino Detector at the LHC,” [arXiv:2210.02784 \[hep-ex\]](https://arxiv.org/abs/2210.02784).

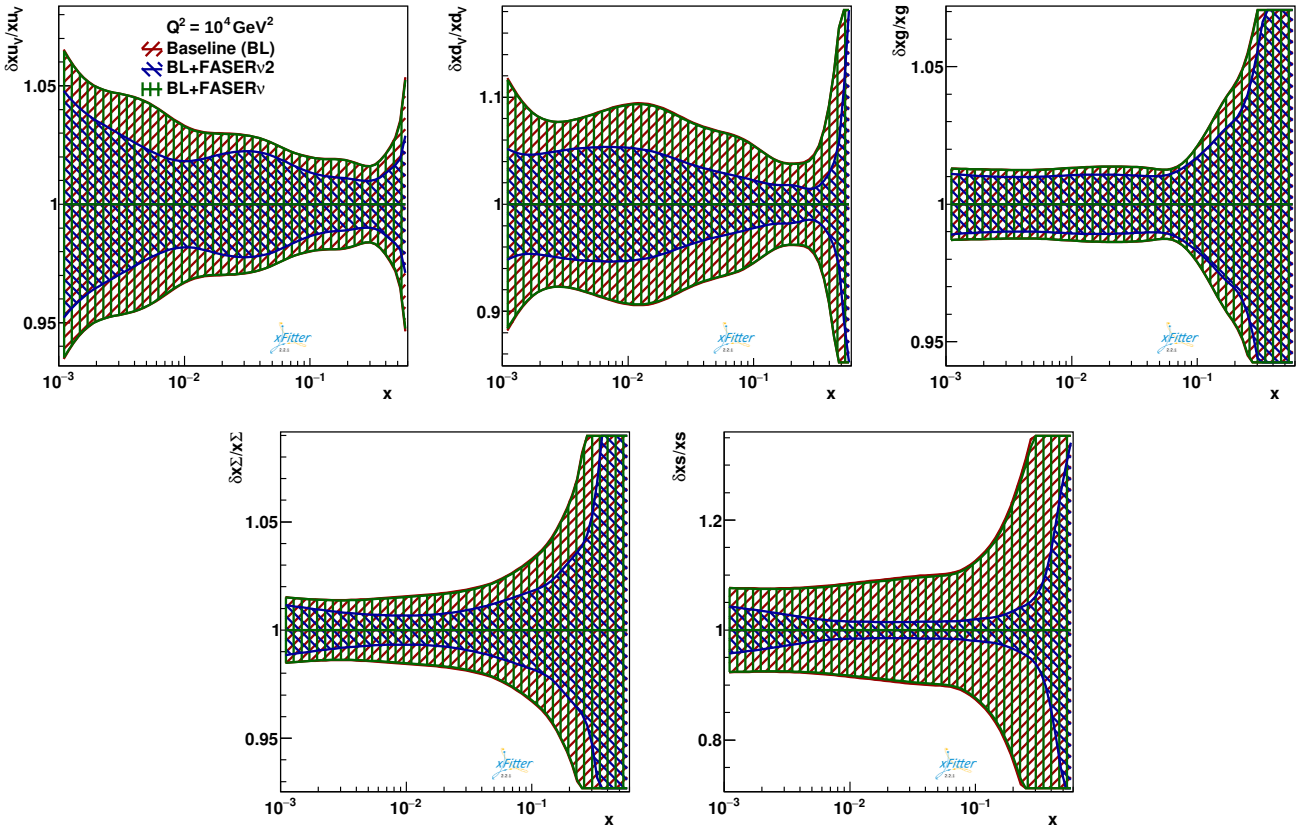


**Fig. A.1.** Same as Fig. 3.1 (statistical uncertainties only), comparing the projected PDF impact of FASER $\nu$ 2 with that of FASER $\nu$ , in the latter case assuming the Run III integrated luminosity of  $\mathcal{L} = 150 \text{ fb}^{-1}$ .

9. L. A. Anchordoqui et al., “The Forward Physics Facility: Sites, experiments, and physics potential,” *Phys. Rept.* **968** (2022) 1–50, [arXiv:2109.10905 \[hep-ph\]](#).
10. J. L. Feng et al., “The Forward Physics Facility at the High-Luminosity LHC,” *J. Phys. G* **50** no. 3, (2023) 030501, [arXiv:2203.05090 \[hep-ex\]](#).
11. P. Azzi et al., “Report from Working Group 1: Standard Model Physics at the HL-LHC and HE-LHC,” *CERN Yellow Rep. Monogr.* **7** (2019) 1–220, [arXiv:1902.04070 \[hep-ph\]](#).
12. M. Cepeda et al., “Report from Working Group 2: Higgs Physics at the HL-LHC and HE-LHC,” *CERN Yellow Rep. Monogr.* **7** (2019) 221–584, [arXiv:1902.00134 \[hep-ph\]](#).
13. J. M. Conrad, M. H. Shaevitz, and T. Bolton, “Precision measurements with high-energy neutrino beams,” *Rev. Mod. Phys.* **70** (1998) 1341–1392, [arXiv:hep-ex/9707015](#).
14. M. L. Mangano et al., “Physics at the front end of a neutrino factory: A Quantitative appraisal,” [arXiv:hep-ph/0105155](#).
15. A. Candido, A. Garcia, G. Magni, T. Rabemananjara, J. Rojo, and R. Stegeman, “Neutrino Structure Functions from GeV to EeV Energies,” *JHEP* **05** (2023) 149, [arXiv:2302.08527 \[hep-ph\]](#).
16. J. J. Ethier and E. R. Nocera, “Parton Distributions in Nucleons and Nuclei,” *Ann. Rev. Nucl. Part. Sci.* **70** (2020) 43–76, [arXiv:2001.07722 \[hep-ph\]](#).
17. J. Gao, L. Harland-Lang, and J. Rojo, “The Structure of the Proton in the LHC Precision Era,” *Phys. Rept.* **742** (2018) 1–121, [arXiv:1709.04922 \[hep-ph\]](#).
18. K. Kovářík, P. M. Nadolsky, and D. E. Soper, “Hadronic structure in high-energy collisions,” *Rev. Mod. Phys.* **92** no. 4, (2020) 045003, [arXiv:1905.06957 \[hep-ph\]](#).
19. NuTeV Collaboration, D. Mason et al., “Measurement of the Nucleon Strange-Antistrange Asymmetry at Next-to-Leading Order in QCD from NuTeV Dimuon Data,” *Phys. Rev. Lett.* **99** (2007) 192001.
20. CCFR Collaboration, A. O. Bazarko et al., “Determination of the strange quark content of the nucleon from a next-to-leading order QCD analysis of neutrino charm production,” *Z. Phys. C* **65** (1995) 189–198, [arXiv:hep-ex/9406007](#).
21. F. Faura, S. Iranipour, E. R. Nocera, J. Rojo, and M. Ubiali, “The Strangest Proton?,” *Eur. Phys. J. C* **80** no. 12, (2020) 1168, [arXiv:2009.00014 \[hep-ph\]](#).
22. S. Alekhin, J. Blumlein, L. Caminada, K. Lipka, K. Lohwasser, S. Moch, R. Pettit, and R. Placakyte, “Determination of Strange Sea Quark Distributions from Fixed-target and Collider Data,” *Phys. Rev. D* **91** no. 9, (2015) 094002, [arXiv:1404.6469 \[hep-ph\]](#).
23. CHORUS Collaboration, G. Onengut et al., “Measurement of nucleon structure functions in neutrino scattering,” *Phys. Lett. B* **632** (2006) 65–75.
24. NuTeV Collaboration, M. Goncharov et al., “Precise Measurement of Dimuon Production Cross-Sections in  $\nu_\mu$

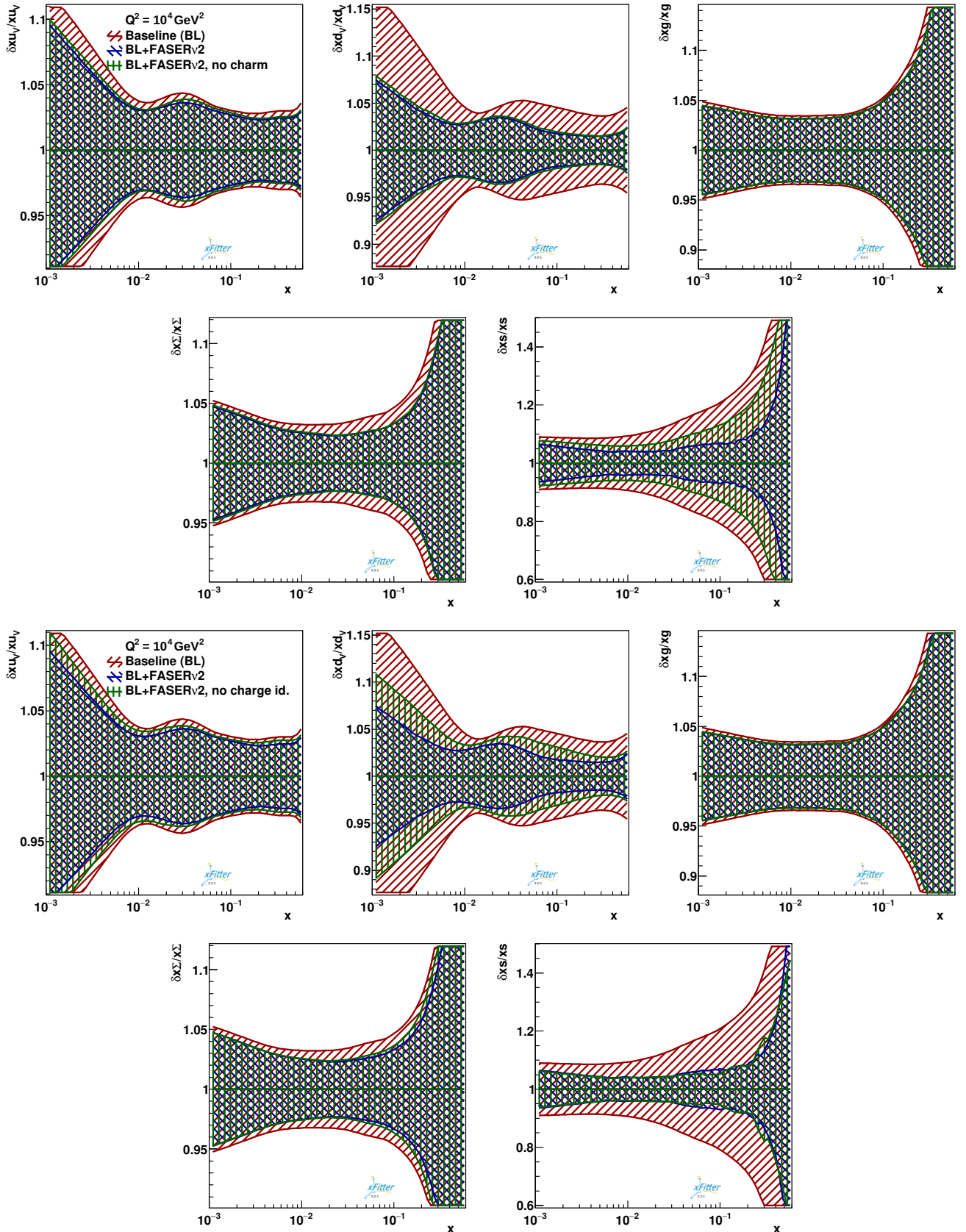


**Fig. B.1.** Same as Fig. 3.2 (upper panels) and Fig. 3.3 (bottom panels) in the case of EPPS21.

- Fe and  $\bar{\nu}_\mu$  Fe Deep Inelastic Scattering at the Tevatron.,” *Phys. Rev. D* **64** (2001) 112006, [arXiv:hep-ex/0102049](#).
25. CCFR/NuTeV Collaboration, U.-K. Yang et al., “Measurements of  $F_2$  and  $xF_3^Y - xF_3^P$  from CCFR  $\nu_\mu$ -Fe and  $\bar{\nu}_\mu$ -Fe data in a physics model independent way,” *Phys. Rev. Lett.* **86** (2001) 2742–2745, [arXiv:hep-ex/0009041 \[hep-ex\]](#).
26. NOMAD Collaboration, O. Samoylov et al., “A Precision Measurement of Charm Dimuon Production in Neutrino Interactions from the NOMAD Experiment,” *Nucl. Phys. B* **876** (2013) 339–375, [arXiv:1308.4750 \[hep-ex\]](#).
27. J. P. Berge et al., “A Measurement of Differential Cross-Sections and Nucleon Structure Functions in Charged Current Neutrino Interactions on Iron,” *Z. Phys. C* **49** (1991) 187–224.
28. NNPDF Collaboration, R. D. Ball et al., “The path to proton structure at 1% accuracy,” *Eur. Phys. J. C* **82** no. 5, (2022) 428, [arXiv:2109.02653 \[hep-ph\]](#).
29. T.-J. Hou et al., “New CTEQ global analysis of quantum chromodynamics with high-precision data from the LHC,” *Phys. Rev. D* **103** no. 1, (2021) 014013, [arXiv:1912.10053 \[hep-ph\]](#).
30. S. Bailey, T. Cridge, L. A. Harland-Lang, A. D. Martin, and R. S. Thorne, “Parton distributions from LHC, HERA, Tevatron and fixed target data: MSHT20 PDFs,” *Eur. Phys. J. C* **81** no. 4, (2021) 341, [arXiv:2012.04684 \[hep-ph\]](#).
31. K. J. Eskola, P. Paakkinen, H. Paukkunen, and C. A. Salgado, “EPPS21: a global QCD analysis of nuclear PDFs,” *Eur. Phys. J. C* **82** no. 5, (2022) 413, [arXiv:2112.12462 \[hep-ph\]](#).
32. R. Abdul Khalek, R. Gauld, T. Giani, E. R. Nocera, T. R. Rabemananjara, and J. Rojo, “nNNPDF3.0: evidence for a modified partonic structure in heavy nuclei,” *Eur. Phys. J. C* **82** no. 6, (2022) 507, [arXiv:2201.12363 \[hep-ph\]](#).
33. K. F. Muzakka et al., “Compatibility of neutrino DIS data and its impact on nuclear parton distribution functions,” *Phys. Rev. D* **106** no. 7, (2022) 074004, [arXiv:2204.13157 \[hep-ph\]](#).
34. R. Abdul Khalek, S. Bailey, J. Gao, L. Harland-Lang, and J. Rojo, “Towards Ultimate Parton Distributions at the High-Luminosity LHC,” *Eur. Phys. J. C* **78** no. 11, (2018) 962, [arXiv:1810.03639 \[hep-ph\]](#).
35. R. Abdul Khalek et al., “Science Requirements and Detector Concepts for the Electron-Ion Collider: EIC Yellow Report,” *Nucl. Phys. A* **1026** (2022) 122447, [arXiv:2103.05419 \[physics.ins-det\]](#).
36. R. A. Khalek, J. J. Ethier, E. R. Nocera, and J. Rojo, “Self-consistent determination of proton and nuclear PDFs at the Electron Ion Collider,” *Phys. Rev. D* **103** no. 9, (2021) 096005, [arXiv:2102.00018 \[hep-ph\]](#).
37. NNPDF Collaboration, R. Abdul Khalek, J. J. Ethier, and J. Rojo, “Nuclear parton distributions from lepton-nucleus scattering and the impact of an electron-ion collider,” *Eur. Phys. J. C* **79** no. 6, (2019) 471, [arXiv:1904.00018 \[hep-ph\]](#).
38. R. Abdul Khalek, S. Bailey, J. Gao, L. Harland-Lang, and J. Rojo, “Probing Proton Structure at the Large Hadron electron Collider,” *SciPost Phys.* **7** no. 4, (2019) 051, [arXiv:1906.10127 \[hep-ph\]](#).
39. LHeC, FCC-he Study Group Collaboration, P. Agostini et al., “The Large Hadron-Electron Collider at the HL-LHC,” *J. Phys. G* **48** no. 11, (2021) 110501, [arXiv:2007.14491 \[hep-ex\]](#).
40. LHeC Study Group Collaboration, J. L. Abelleira Fernandez et al., “A Large Hadron Electron Collider at CERN: Report on the Physics and Design Concepts for Machine and Detector,” *J. Phys. G* **39** (2012) 075001, [arXiv:1206.2913 \[physics.acc-ph\]](#).
41. B. Batell, J. L. Feng, and S. Trojanowski, “Detecting Dark Matter with Far-Forward Emulsion and Liquid Argon Detectors at the LHC,” *Phys. Rev. D* **103** no. 7, (2021) 075023, [arXiv:2101.10338 \[hep-ph\]](#).
42. B. Batell, J. L. Feng, A. Ismail, F. Kling, R. M. Abraham, and S. Trojanowski, “Discovering dark matter at the LHC through its nuclear scattering in far-forward emulsion and liquid argon detectors,” *Phys. Rev. D* **104** no. 3, (2021) 035036, [arXiv:2107.00666 \[hep-ph\]](#).
43. H. Paukkunen and P. Zurita, “PDF reweighting in the Hessian matrix approach,” *JHEP* **12** (2014) 100, [arXiv:1402.6623 \[hep-ph\]](#).
44. C. Schmidt, J. Pumplin, C. P. Yuan, and P. Yuan, “Updating and optimizing error parton distribution function sets in the Hessian approach,” *Phys. Rev. D* **98** no. 9, (2018) 094005, [arXiv:1806.07950 \[hep-ph\]](#).
45. HERAFitter developers’ team Collaboration, S. Camarda et al., “QCD analysis of  $W$ - and  $Z$ -boson production at Tevatron,” *Eur. Phys. J. C* **75** no. 9, (2015) 458, [arXiv:1503.05221 \[hep-ph\]](#).
46. PDF4LHC Working Group Collaboration, R. D. Ball et al., “The PDF4LHC21 combination of global PDF fits for the LHC Run III,” *J. Phys. G* **49** no. 8, (2022) 080501, [arXiv:2203.05506 \[hep-ph\]](#).
47. S. Alekhin et al., “HERAFitter,” *Eur. Phys. J. C* **75** no. 7, (2015) 304, [arXiv:1410.4412 \[hep-ph\]](#).
48. V. Bertone, M. Botje, D. Britzger, et al., “xFitter 2.0.0: An open source QCD fit framework,” *PoS DIS2017* (2018) 203, [arXiv:1709.01151 \[hep-ph\]](#).
49. xFitter Collaboration, H. Abdolmaleki et al., “xFitter: An Open Source QCD Analysis Framework. A resource and reference document for the Snowmass study,” 6, 2022, [arXiv:2206.12465 \[hep-ph\]](#).
50. xFitter Developers’ Team. <https://www.xfitter.org/xFitter/>.
51. NNPDF Collaboration, R. D. Ball et al., “An open-source machine learning framework for global analyses of parton distributions,” *Eur. Phys. J. C* **81** no. 10, (2021) 958, [arXiv:2109.02671 \[hep-ph\]](#).
52. J. Gao, “Massive charged-current coefficient functions in deep-inelastic scattering at NNLO and impact on strange-quark distributions,” *JHEP* **02** (2018) 026, [arXiv:1710.04258 \[hep-ph\]](#).
53. A. Candido, F. Hekhorn, and G. Magni, “EKO: evolution kernel operators,” *Eur. Phys. J. C* **82** no. 10, (2022) 976, [arXiv:2202.02338 \[hep-ph\]](#).
54. A. Candido and F. Hekhorn, “YADISM: Yet Another DIS Module,” in preparation (2023).
55. S. Carrazza, E. R. Nocera, C. Schwan, and M. Zaro, “PineAPPL: combining EW and QCD corrections for fast evaluation of LHC processes,” *JHEP* **12** (2020) 108, [arXiv:2008.12789 \[hep-ph\]](#).
56. R. S.ufian, T. Liu, G. F. de Téramond, H. G. Dosch, S. J. Brodsky, A. Deur, M. T. Islam, and B.-Q. Ma, “Nonperturbative strange-quark sea from lattice QCD, light-front holography, and meson-baryon fluctuation models,” *Phys. Rev. D* **98** no. 11, (2018) 114004, [arXiv:1809.04975 \[hep-ph\]](#).

57. R. S. Sufian, T. Liu, A. Alexandru, S. J. Brodsky, G. F. de Téramond, H. G. Dosch, T. Draper, K.-F. Liu, and Y.-B. Yang, “Constraints on charm-anticharm asymmetry in the nucleon from lattice QCD,” *Phys. Lett. B* **808** (2020) 135633, [arXiv:2003.01078 \[hep-lat\]](https://arxiv.org/abs/2003.01078).
58. R. D. Ball, E. R. Nocera, and R. L. Pearson, “Deuteron Uncertainties in the Determination of Proton PDFs,” *Eur. Phys. J. C* **81** no. 1, (2021) 37, [arXiv:2011.00009 \[hep-ph\]](https://arxiv.org/abs/2011.00009).
59. NNPDF Collaboration, R. D. Ball, E. R. Nocera, and R. L. Pearson, “Nuclear Uncertainties in the Determination of Proton PDFs,” *Eur. Phys. J. C* **79** no. 3, (2019) 282, [arXiv:1812.09074 \[hep-ph\]](https://arxiv.org/abs/1812.09074).
60. NNPDF Collaboration, R. Abdul Khalek et al., “A first determination of parton distributions with theoretical uncertainties,” *Eur. Phys. J. C* (2019) 79:838, [arXiv:1905.04311 \[hep-ph\]](https://arxiv.org/abs/1905.04311).
61. NNPDF Collaboration, R. Abdul Khalek et al., “Parton Distributions with Theory Uncertainties: General Formalism and First Phenomenological Studies,” *Eur. Phys. J. C* **79** no. 11, (2019) 931, [arXiv:1906.10698 \[hep-ph\]](https://arxiv.org/abs/1906.10698).
62. FASER Collaboration, A. Ariga et al., “FASER: ForwArd Search ExpeRiment at the LHC,” [arXiv:1901.04468 \[hep-ex\]](https://arxiv.org/abs/1901.04468).
63. Aachen-Bonn-CERN-Munich-Oxford Collaboration, P. Allen et al., “Multiplicity Distributions in Neutrino - Hydrogen Interactions,” *Nucl. Phys. B* **181** (1981) 385–402.
64. P. Nason, “A New method for combining NLO QCD with shower Monte Carlo algorithms,” *JHEP* **11** (2004) 040, [arXiv:hep-ph/0409146](https://arxiv.org/abs/hep-ph/0409146).
65. S. Frixione, P. Nason, and C. Oleari, “Matching NLO QCD computations with Parton Shower simulations: the POWHEG method,” *JHEP* **11** (2007) 070, [arXiv:0709.2092 \[hep-ph\]](https://arxiv.org/abs/0709.2092).
66. S. Alioli, P. Nason, C. Oleari, and E. Re, “A general framework for implementing NLO calculations in shower Monte Carlo programs: the POWHEG BOX,” *JHEP* **06** (2010) 043, [arXiv:1002.2581 \[hep-ph\]](https://arxiv.org/abs/1002.2581).
67. T. Sjöstrand, S. Ask, J. R. Christiansen, R. Corke, N. Desai, P. Ilten, S. Mrenna, S. Prestel, C. O. Rasmussen, and P. Z. Skands, “An introduction to PYTHIA 8.2,” *Comput. Phys. Commun.* **191** (2015) 159–177, [arXiv:1410.3012 \[hep-ph\]](https://arxiv.org/abs/1410.3012).
68. C. Bierlich et al., “A comprehensive guide to the physics and usage of PYTHIA 8.3” [arXiv:2203.11601 \[hep-ph\]](https://arxiv.org/abs/2203.11601).
69. T. Pierog, I. Karpenko, J. M. Katzy, E. Yatsenko, and K. Werner, “EPOS LHC: Test of collective hadronization with data measured at the CERN Large Hadron Collider,” *Phys. Rev. C* **92** no. 3, (2015) 034906, [arXiv:1306.0121 \[hep-ph\]](https://arxiv.org/abs/1306.0121).
70. L. Buonocore, F. Kling, L. Rottoli, and J. Sominka, “Predictions for Neutrinos and New Physics from Forward Heavy Hadron Production at the LHC.” In preparation, 2023.
71. F. Kling, T. Mäkelä, and S. Trojanowski, “Investigating the fluxes and physics potential of LHC neutrino experiments,” [arXiv:2309.10417 \[hep-ph\]](https://arxiv.org/abs/2309.10417).
72. M. Fieg, F. Kling, H. Schulz, and T. Sjöstrand, “Tuning Pythia for Forward Physics Experiments,” [arXiv:2309.08604 \[hep-ph\]](https://arxiv.org/abs/2309.08604).
73. S. Amoroso et al., “Compatibility and combination of world W-boson mass measurements,” [arXiv:2308.09417 \[hep-ex\]](https://arxiv.org/abs/2308.09417).
74. R. D. Ball, A. Candido, S. Forte, F. Hekhorn, E. R. Nocera, J. Rojo, and C. Schwan, “Parton distributions and new physics searches: the Drell-Yan forward-backward asymmetry as a case study,” *Eur. Phys. J. C* **82** no. 12, (2022) 1160, [arXiv:2209.08115 \[hep-ph\]](https://arxiv.org/abs/2209.08115).
75. J. J. Ethier, R. Gomez-Ambrosio, G. Magni, and J. Rojo, “SMEFT analysis of vector boson scattering and diboson data from the LHC Run II,” *Eur. Phys. J. C* **81** no. 6, (2021) 560, [arXiv:2101.03180 \[hep-ph\]](https://arxiv.org/abs/2101.03180).
76. A. Greljo, S. Iranipour, Z. Kassabov, M. Madigan, J. Moore, J. Rojo, M. Ubiali, and C. Voisey, “Parton distributions in the SMEFT from high-energy Drell-Yan tails,” *JHEP* **07** (2021) 122, [arXiv:2104.02723 \[hep-ph\]](https://arxiv.org/abs/2104.02723).
77. C. Schwan, A. Candido, F. Hekhorn, S. Carrazza, and A. Barontini, “Nnpdf/pineappl: v0.6.0,” Zenodo, June, 2023. <https://doi.org/10.5281/zenodo.7995675>.
78. S. Forte, E. Laenen, P. Nason, and J. Rojo, “Heavy quarks in deep-inelastic scattering,” *Nucl. Phys. B* **834** (2010) 116–162, [arXiv:1001.2312 \[hep-ph\]](https://arxiv.org/abs/1001.2312).
79. R. D. Ball, V. Bertone, F. Cerutti, L. Del Debbio, S. Forte, A. Guffanti, J. I. Latorre, J. Rojo, and M. Ubiali, “Impact of Heavy Quark Masses on Parton Distributions and LHC Phenomenology,” *Nucl. Phys. B* **849** (2011) 296–363, [arXiv:1101.1300 \[hep-ph\]](https://arxiv.org/abs/1101.1300).
80. R. D. Ball, L. Del Debbio, S. Forte, A. Guffanti, J. I. Latorre, J. Rojo, and M. Ubiali, “A first unbiased global NLO determination of parton distributions and their uncertainties,” *Nucl. Phys. B* **838** (2010) 136–206, [arXiv:1002.4407 \[hep-ph\]](https://arxiv.org/abs/1002.4407).
81. A. Barontini, A. Candido, J. M. Cruz-Martinez, F. Hekhorn, and C. Schwan, “Pineline: Industrialization of High-Energy Theory Predictions,” [arXiv:2302.12124 \[hep-ph\]](https://arxiv.org/abs/2302.12124).
82. G. Watt and R. S. Thorne, “Study of Monte Carlo approach to experimental uncertainty propagation with MSTW 2008 PDFs,” *JHEP* **08** (2012) 052, [arXiv:1205.4024 \[hep-ph\]](https://arxiv.org/abs/1205.4024).
83. S. Carrazza, J. I. Latorre, J. Rojo, and G. Watt, “A compression algorithm for the combination of PDF sets,” *Eur. Phys. J. C* **75** (2015) 474, [arXiv:1504.06469 \[hep-ph\]](https://arxiv.org/abs/1504.06469).
84. NNPDF Collaboration, R. D. Ball et al., “Parton distributions from high-precision collider data,” *Eur. Phys. J. C* **77** no. 10, (2017) 663, [arXiv:1706.00428 \[hep-ph\]](https://arxiv.org/abs/1706.00428).
85. J. Gao and P. Nadolsky, “A meta-analysis of parton distribution functions,” *JHEP* **07** (2014) 035, [arXiv:1401.0013 \[hep-ph\]](https://arxiv.org/abs/1401.0013).
86. S. Carrazza, S. Forte, Z. Kassabov, J. I. Latorre, and J. Rojo, “An Unbiased Hessian Representation for Monte Carlo PDFs,” *Eur. Phys. J. C* **75** no. 8, (2015) 369, [arXiv:1505.06736 \[hep-ph\]](https://arxiv.org/abs/1505.06736).
87. S. Carrazza, S. Forte, Z. Kassabov, and J. Rojo, “Specialized minimal PDFs for optimized LHC calculations,” *Eur. Phys. J. C* **76** no. 4, (2016) 205, [arXiv:1602.00005 \[hep-ph\]](https://arxiv.org/abs/1602.00005).
88. NNPDF Collaboration, R. D. Ball, V. Bertone, M. Bonvini, S. Carrazza, S. Forte, A. Guffanti, N. P. Hartland, J. Rojo, and L. Rottoli, “A Determination of the Charm Content of the Proton,” *Eur. Phys. J. C* **76** no. 11, (2016) 647, [arXiv:1605.06515 \[hep-ph\]](https://arxiv.org/abs/1605.06515).

89. **NNPDF** Collaboration, R. D. Ball, A. Candido, J. Cruz-Martinez, S. Forte, T. Giani, F. Hekhorn, K. Kudashkin, G. Magni, and J. Rojo, “Evidence for intrinsic charm quarks in the proton,” *Nature* **608** no. 7923, (2022) 483–487, [arXiv:2208.08372 \[hep-ph\]](https://arxiv.org/abs/2208.08372).
90. P. Duwentäster, T. Ježo, M. Klasen, K. Kovařík, A. Kusina, K. F. Muzakka, F. I. Olness, R. Ruiz, I. Schienbein, and J. Y. Yu, “Impact of heavy quark and quarkonium data on nuclear gluon PDFs,” *Phys. Rev. D* **105** no. 11, (2022) 114043, [arXiv:2204.09982 \[hep-ph\]](https://arxiv.org/abs/2204.09982).
91. R. Frederix, S. Frixione, V. Hirschi, D. Pagani, H. S. Shao, and M. Zaro, “The automation of next-to-leading order electroweak calculations,” *JHEP* **07** (2018) 185, [arXiv:1804.10017 \[hep-ph\]](https://arxiv.org/abs/1804.10017).
92. Y. S. Jeong and M. H. Reno, “Neutrino Cross Sections: Interface of shallow- and deep-inelastic scattering for collider neutrinos,” [arXiv:2307.09241 \[hep-ph\]](https://arxiv.org/abs/2307.09241).
93. J. Cruz-Martinez, M. Fieg, T. Giani, P. Krack, T. Makela, T. Rabemananjara, and J. Rojo, “Lhcfitnikhef/fpf-wg1,” Sept., 2023. <https://doi.org/10.5281/zenodo.8355209>.
94. A. Buckley, J. Ferrando, S. Lloyd, K. Nordström, B. Page, M. Rüfenacht, M. Schönherr, and G. Watt, “LHAPDF6: parton density access in the LHC precision era,” *Eur. Phys. J. C* **75** (2015) 132, [arXiv:1412.7420 \[hep-ph\]](https://arxiv.org/abs/1412.7420).